Ore Geology Reviews 114 (2019) 103135

Contents lists available at ScienceDirect

Ore Geology Reviews

journal homepage: www.elsevier.com/locate/oregeorev

The origin of CH_4-rich fluids in reduced porphyry–skarn Cu–Mo–Au systems

Wei Zhang[a], Anthony E. Williams-Jones[b], Cheng-Biao Leng[a,c,*], Xing-Chun Zhang[a,*], Wei Terry Chen[a], Chao-Jian Qin[a], Wen-Chao Su[a], Jia-Hui Yan[d]

[a] State Key Laboratory of Ore Deposit Geochemistry, Institute of Geochemistry Chinese Academy of Sciences, Guiyang 550081, China
[b] Department of Earth and Planetary Sciences, McGill University, Québec H3A OE8, Canada
[c] State Key Laboratory of Nuclear Resources and Environment, East China University of Technology, Nanchang 330013, China
[d] Central South Geo-Exploration Institute, China Metallurgical Geology Bureau, Wuhan 430081, China

ARTICLE INFO

Keywords:
Fluid inclusions
Raman spectroscopy
Methane
Abiogenic
Reduction
Seleteguole

ABSTRACT

Although most of the methane on Earth is of biogenic origin, significant abiogenic methane has been identified in a variety of geological environments. Moreover, the presence of methane has been reported recently in fluid inclusions from a number of reduced porphyry deposits. The genesis of this methane, however, remains poorly understood. Here, we present results of a study of magma-exsolved CH_4-rich aqueous fluid inclusions in the Seleteguole reduced porphyry–skarn Cu–Mo–Au deposit, NW China. Four types of fluid inclusions, namely intermediate-density two-phase aqueous inclusions, low-density vapor inclusions, brine inclusions and aqueous liquid inclusions, have been distinguished on the basis of the phases present at room temperature. The intermediate-density inclusions were trapped as a single phase and contain 3.8–10.4 mol/kg CH_4, corresponding to an oxygen fugacity between ΔFMQ − 1 and ΔFMQ − 0.5. This attests to the remarkably reduced nature of the fluid. The $\delta^{13}C$ value of the CH_4-hosted fluid inclusions ranges from –29.4‰ to –19.1‰ (PDB), which distinguishes this methane from biogenic methane. Indeed, the high homogenization temperature of the CH_4-rich inclusions (~400 °C) implies that the CH_4 was exsolved directly from the magma. Given the environment in which the magma was likely generated, i.e., at or immediately above a subducting plate, we propose that the methane was produced by reactions involving organic matter-bearing carbonate rocks in the subduction zone. Although Cu, Mo and Au in most porphyry systems are interpreted to have been transported under oxidizing conditions, our results indicate that reduced aqueous liquids and vapors are also capable of transporting appreciable concentrations of these metals.

1. Introduction

Methane (CH_4), the most abundant reduced carbonic species on Earth, occurs in oil fields and coal beds, is a component of gas hydrates, and is commonly reported in analyses of fluid inclusions (e.g., Hall and Bodnar, 1990; Dubessy et al., 2001; Potter and Konnerup-Madsen, 2003; Sherwood Lollar et al., 2006). It may have contributed to the origin of life directly as a building block for the synthesis of complex organic molecules and indirectly as one of the greenhouse gases that kept temperatures high enough to sustain life (Zahnle, 1986; Fiebig et al., 2007). Although most of the Earth's methane is sourced from biogenic materials during burial and/or diagenesis in sedimentary rocks (Schoell, 1988; Sherwood Lollar et al., 2002), it can also be produced together with higher hydrocarbons by several abiogenic processes including those associated with magmatism (Schoell, 1988; Salvi and Williams-Jones, 1997; Sherwood Lollar et al., 2002; Potter and Konnerup-Madsen, 2003; Fiebig et al., 2007; Etiope and Sherwood Lollar, 2013; Vasyukova et al., 2016).

Recently, CH_4-bearing fluid inclusions have been identified in a significant number of porphyry- and/or skarn-type deposits (e.g., Rowins, 2000; Shen et al., 2010; Zhu et al., 2012; Cao et al., 2014; Wang et al., 2014; Ren and Ma, 2015). Indeed, the presence of a CH_4-bearing fluid is considered to be one of the diagnostic features of reduced porphyry copper deposits (RPCDs), which are generally of small to medium size but rich in gold (e.g., Rowins, 2000; Smith et al., 2012; Cao et al., 2014). The origin of the CH_4 and its potential role in the mineralization, however, are still poorly understood. The few studies that have considered the origin of the CH_4, with one exception, have attributed it to the interaction of the magmas and/or hydrothermal fluids with carbonaceous sediments (e.g., Zhu et al. 2012; Shen and

* Corresponding authors at: State Key Laboratory of Ore Deposit Geochemistry, Institute of Geochemistry Chinese Academy of Sciences, Guiyang 550081, China (C.-B. Leng).
E-mail addresses: lengchengbiao@vip.gyig.ac.cn (C.-B. Leng), zhangxingchun@vip.gyig.ac.cn (X.-C. Zhang).

https://doi.org/10.1016/j.oregeorev.2019.103135
Received 19 April 2019; Received in revised form 2 September 2019; Accepted 19 September 2019
Available online 20 September 2019

Pan, 2013; Ren and Ma, 2015). The exception is the study by Cao et al. (2014) of the Baogutu deposit, China, who proposed that the CH_4 was produced by a Fischer–Tropsch synthesis during sodic and potassic hydrothermal alteration.

In this paper, we report results of a study of CH_4-rich fluid inclusions in the Seleteguole Cu–Mo–Au deposit, China. These fluid inclusions are interpreted to be primary (except where hosted by quartz phenocrysts), and thus are considered to provide direct evidence for the exsolution of CH_4-bearing ore fluid from magma. Based on the results of detailed petrographic, microthermometric, Raman spectroscopic and carbon isotopic analyses of the fluid inclusions, we propose that the CH_4 was introduced into the magma from methanogenesis in the subduction zone. We further propose that the reduced nature of the ore fluid favored the transport of Au over Cu, thereby satisfactorily explaining the gold enrichment of the Seleteguole deposit and other RCPDs. The insights gained in this study will provide the basis for developing a comprehensive model for the genesis of RCPDs that will help guide exploration for this important subclass of porphyry deposits.

2. Geological setting

The Western Tianshan is located in northwestern China and separates the Junggar Basin to the north and the Tarim Basin to the south (Fig. 1a). Tectonically, the Western Tianshan can be subdivided from north to south into the Northern, Central and Southern Tianshan belts (Xiao et al., 2013), which are separated by the Northern Tianshan and the Southern Tianshan sutures, respectively (Fig. 1a). The Northwestern Tianshan is generally regarded to be a Late Paleozoic continental arc developed on the Yili Block in response to the subduction of the Junggar plate (Gao et al., 1998; Wang et al., 2007; Xiao et al., 2013). It is composed mainly of Precambrian metamorphic basement, Cambrian to Ordovician epicontinental siliciclastic and carbonate rocks and Devonian to Carboniferous clastic sedimentary and volcanic rocks (Fig. 1b; Zuo et al., 2008). Granitoids are widespread in the Northwestern Tianshan and are mostly concentrated in an E–W linear belt (Fig. 1b). They range in age from Neoproterozoic through Early Paleozoic to Late Paleozoic. Neoproterozoic and Early Paleozoic granitoid are distributed in Wenquan area and with zircon ages of 942–798 Ma (Hu et al., 2000, 2010) and 466–447 Ma (Hu et al., 2008), respectively. The Late Paleozoic granitoids are distributed mainly along the northern margin of the Yili block, and are spatially associated with porphyry deposits, such as the Lamasu (Cu–Zn), Dabate (Cu), Lailisigao'er (Cu–Mo) and Seleteguole (Cu–Mo–Au) deposits (e.g., Zhang et al., 2008; Tang et al., 2010; Xue et al., 2011; Zhang et al., 2016).

Seleteguole is a newly-discovered porphyry–skarn Cu–Mo–Au deposit on the northern margin of the Northwestern Tianshan (Fig. 1b). It has a resource of 13,632 tons of Cu (0.12–2.02 wt%), 357 tons of Mo (0.005–0.13 wt%), and 0.5 tons of Au (5.6–22 g/t). The strata in the Seleteguole district belong to the Middle Carboniferous Dongtujin Formation, and consist of thinly to thickly bedded siltstone, siliceous siltstone, calcareous siltstone, calcareous feldspathic sandstone and thinly-bedded limestone (Zhang et al., 2016). Three phases of intrusions, namely pre-mineralization biotite granite, and syn-mineralization diorite porphyry and quartz diorite porphyry (Fig. 2a, b), were emplaced in the carbonate rocks of the Dongtujin Formation. Emplacement of these intrusions led to the development of skarns in the intrusive bodies and the country rocks (Fig. 2c, d). Radiometric determinations using the LA-ICP-MS zircon U-Pb method yielded an age of 307 ± 3 Ma for the biotite granite and an age of 302 ± 3 Ma for both the diorite porphyry and the quartz diorite porphyry (Zhang et al., 2016). Euhedral ilmenite, which represents reduced feature of the rocks, is a common accessory mineral enclosed in the primary biotite (Fig. 2e) or as interstitial phase in rock-forming minerals in these intrusions. Locally, original ilmenite was replaced by titanite at its crystal margins (Fig. 2f). Orebodies in the porphyries are mainly consisted of quartz–chalcopyrite–molybdenite, quartz–chalcopyrite and quartz–molybdenite stockworks, with vein thicknesses ranging from several centimeters to 2 cm (Fig. 2b). Disseminated chalcopyrite and patchy of molybdenite are also observed in the porphyries. Endoskarn, composed mainly of garnet, pyroxene, vesuvianite, wollastonite and quartz, occurs as irregular veins and replacements in the porphyries. Exoskarn, consisting mainly of garnet, pyroxene, vesuvianite, wollastonite, epidote, chlorite, quartz and calcite, is extensively developed at the contacts between the porphyries and limestone and host most of the mineralization (Fig. 2d). The ore minerals in the skarns comprise chalcopyrite, bornite, chalcocite, molybdenite and native gold, whereas the gangue minerals comprise garnet, pyroxene, vesuvianite, wollastonite epidote, quartz and calcite.

3. Methods

Fluid inclusions were studied in over 100 samples collected from outcrops and drill holes. Polished thin sections, approximately 150 μm thick, were prepared from these samples for fluid inclusion petrography, microthermometry and Raman spectroscopic analyses. Several samples with abundant fluid inclusions were selected for carbon isotopic analyses.

3.1. Microthermometry

Measurements of the temperatures of phase changes in the fluid inclusions were conducted on a Linkam THMSG 600 programmable heating–freezing stage mounted on a Leica microscope at the State Key Laboratory of Ore Deposit Geochemistry (SKLODG), Institute of Geochemistry, Chinese Academy of Sciences. The equipment permits the measurement of phase changes for temperatures ranging from −196 to 600 °C and was calibrated using the microthermometric behaviour of synthetic fluid inclusions of known composition. For temperatures below 0 °C, the accuracy of the measurements was about ± 0.1 °C and for temperatures above 200 °C, it was about ± 1 °C.

3.2. Raman spectroscopic analysis

Room temperature Raman spectroscopic analyses of the composition of the fluid inclusion gases were conducted at SKLODG using a Renishaw in Via Reflex Raman microprobe equipped with an argon ion laser having a source of 514 nm. The scanning range for the spectra was set between 0 and 4,500 cm^{-1} and the data accumulation time was 60 s for each scan; the laser beam width was ~1 μm, and the spectral resolution ~0.14 cm^{-1}.

Raman spectroscopic analyses of fluid inclusions heated above the temperature of homogenization were carried out at the Key Laboratory of Tectonics and Petroleum Resources of the Ministry of Education (KLPRME), China University of Geosciences (Wuhan) using a JY/Horiba LabRam HR800 Raman system equipped with a frequency doubled Nd:YAG laser (532.06 nm) having an output laser power of 45 mW, and a 50 × long-work-distance Olympus objective with numerical aperture of 0.5. A Linkam CAP500 heating–cooling stage, containing a high pressure optical capillary cell, was used to homogenize the inclusions for in-situ Raman measurements. Details of the operating conditions for the Raman instrument and the analytical procedures are reported in Ou et al. (2015).

3.3. Carbon isotopes

The $\delta^{13}C_{CH4}$ values were determined using a Thermo Finnigan MAT-253 isotope ratio mass spectrometer at the Analytical Laboratory, Beijing Research Institute of Uranium Geology (ALBRIUG), China. Samples of the host minerals were first washed with dilute HCl in order to remove carbonate and then washed repeatedly with Nanopure water to remove any contaminants from the crystal surfaces. Methane was extracted from the samples by thermally decrepitating the fluid inclusions. This involved

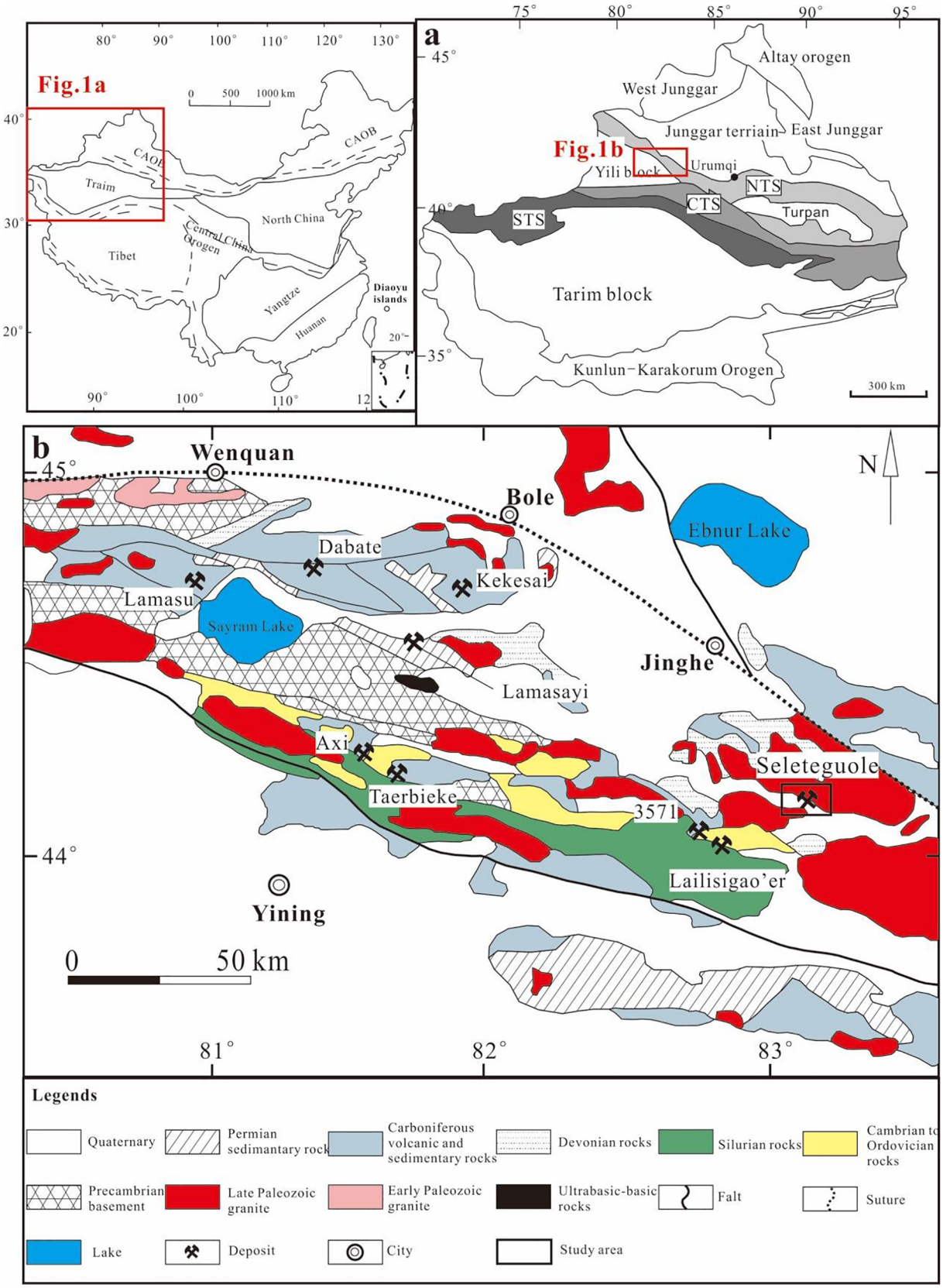

Fig. 1. (a) A simplified geological sketch of the Xinjiang Uygur Autonomous Region and the location of the Northwestern Tianshan, and (b) a geological map of the Northwestern Tianshan (XBGMR, 1993), showing the locations of porphyry copper and epithermal gold deposits in the region. STS = South Tianshan, CTS = Central Tianshan, NTS = North Tianshan.

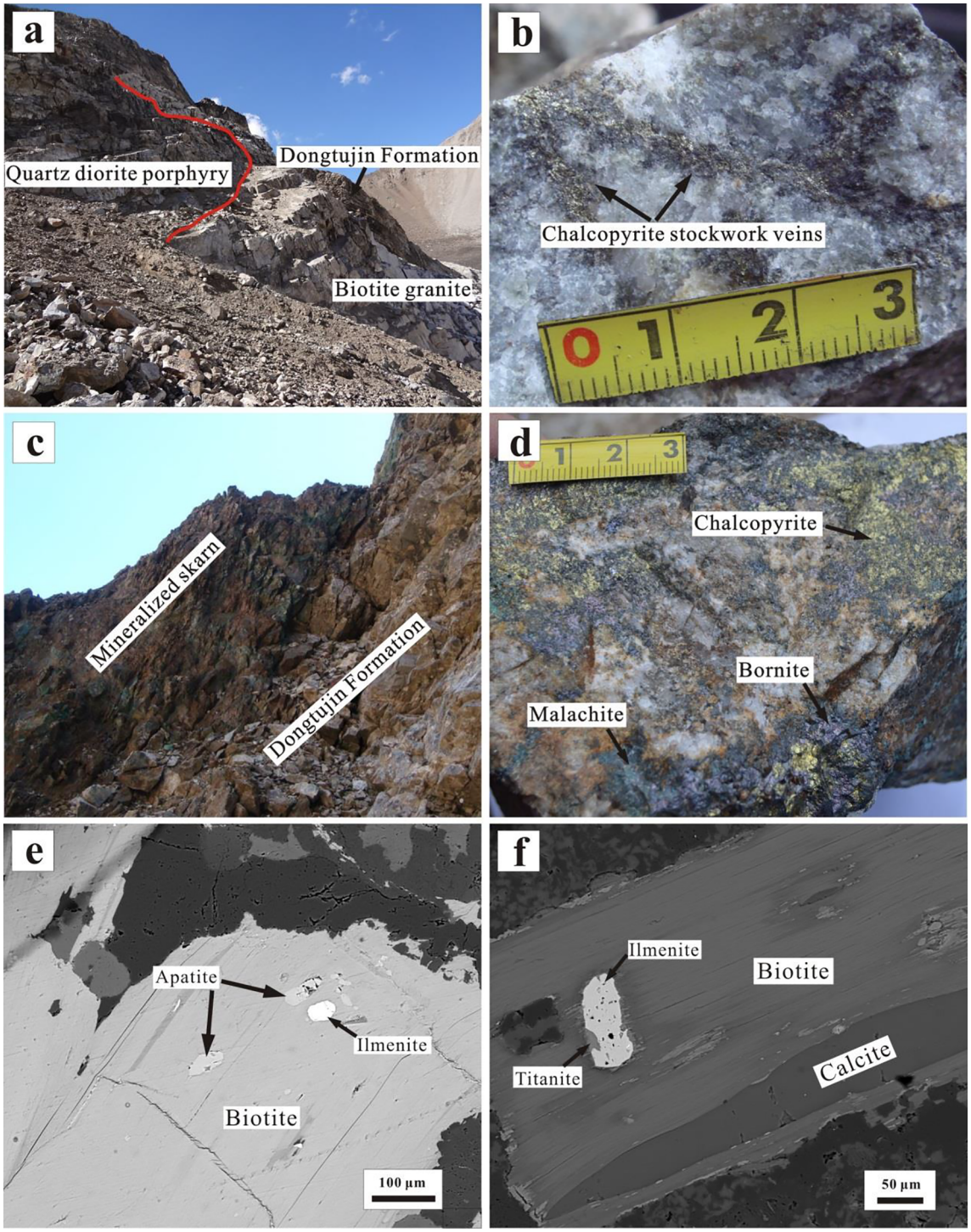

Fig. 2. Field and hand specimen photographs of the Seleteguole porphyry–skarn Cu–Mo–Au deposit. (a) Quartz diorite porphyry and biotite granite stocks in the Dongtujin Formation. (b) Chalcopyrite stockwork veins in the quartz diorite porphyry. (c) A contact zone between the mineralized skarn (the green colored mineral is malachite) and the Dongtujin Formation. (d) A chalcopyrite–bornite–quartz vein in the exoskarn. (e) Backscattered electron images show the occurrence of euhedral ilmenite and apatite inclusions in biotite from the quartz diorite porphyry. (f) Replacement of ilmenite by titanite at the crystal margins in the quartz diorite porphyry. (For interpretation of the references to color in this figure legend, the reader is referred to the web version of this article.)

heating the samples for 15 min under a vacuum at 600 °C. The released CH_4 gas was then oxidized to CO_2 by reaction with Cu_2O and passed through a dry ice + ethanol cold trap followed by a liquid N_2 cold trap to remove the H_2O. The carbon isotope composition of the CO_2 was determined using the mass spectrometer.

The $\delta^{13}C$ of the unaltered limestone and altered marble samples from the Dongtujin Formation were analysed at SKLODG. Small pieces of limestone and marble were taken from whole-rock samples and powdered, and approximately 300 mg of powder was reacted with 100% H_3PO_4 under vacuum for 24 h (25 °C). The resulting CO_2 was analysed for its carbon isotope composition on a Thermo Finnigan MAT-253 isotope ratio mass spectrometer. Calcite GBW 04417, with a $\delta^{13}C$ value of −6.06‰, was used as an external standard. The analytical accuracy was better than ± 0.2‰.

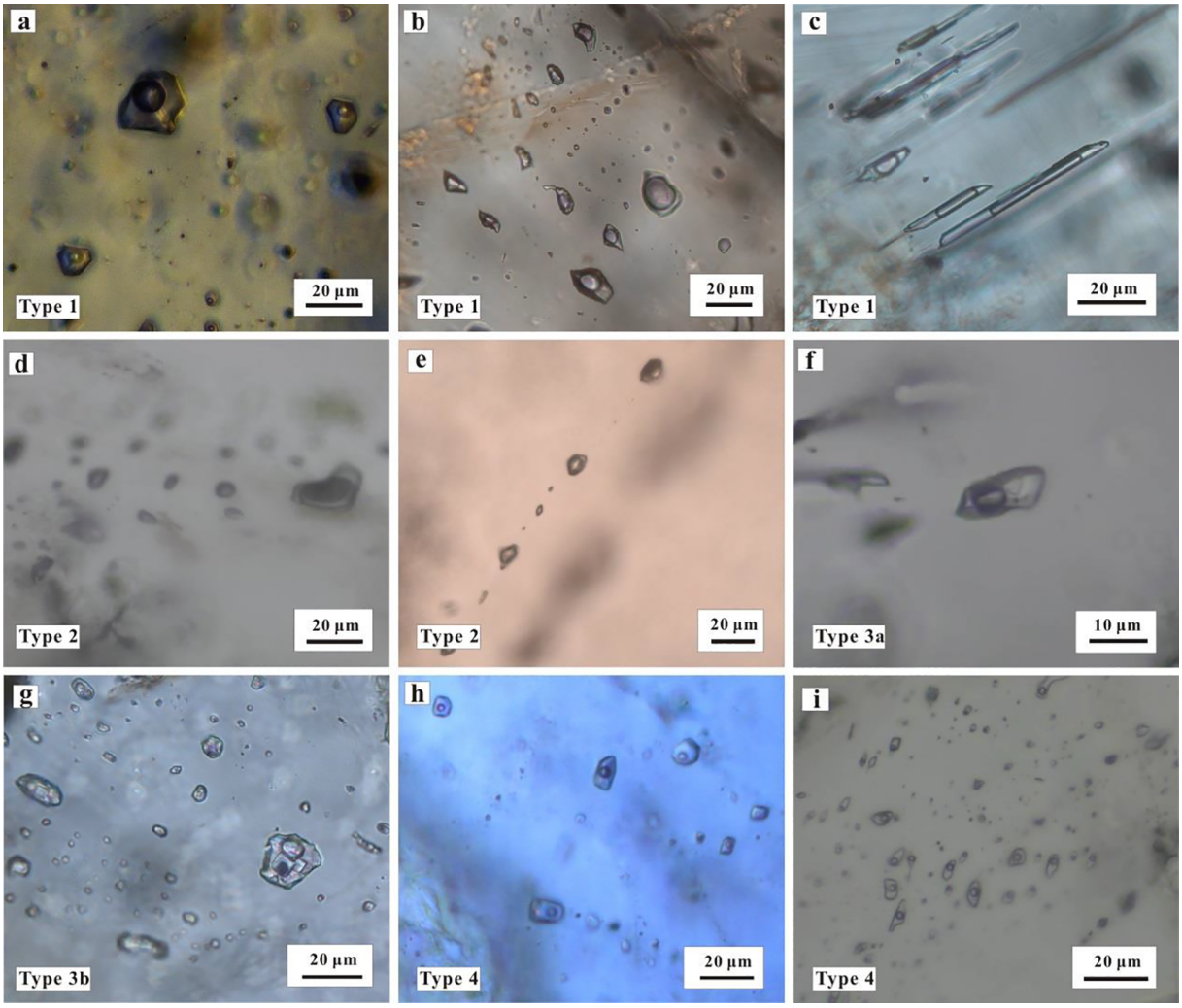

Fig. 3. Photomicrographs of the fluid inclusions in the Seleteguole deposit. (a) Type 1 inclusions irregularly distributed in quartz. (b) Ellipsoidal Type 1 inclusions along a growth zone of garnet. (c) Lenticular Type 1 inclusions along a growth zone in vesuvianite. (d) Type 2 inclusions in garnet. (e) Secondary vapor-rich inclusions distributed as trails along healed fractures in quartz. (f) A Type 3a inclusion containing halite and an opaque solid in vesuvianite. (g) A Type 3b brine inclusion in garnet containing halite and several other solids. (h) Aqueous liquid inclusions scattered distributed in quartz veins in porphyry. (i) Aqueous liquid inclusions distributed as clusters in quartz veins in skarn.

4. Results

4.1. Fluid inclusion petrography

Fluid inclusions were observed in several minerals of the Seleteguole deposit, namely in quartz phenocrysts and vein quartz in the porphyries, garnet and vesuvianite in the prograde skarn, and vein quartz and calcite in the retrograde skarn. The inclusions were subdivided into four types based on the phases and phase ratios observed at room temperature: (1) intermediate-density two-phase aqueous inclusions, (2) low-density vapor inclusions, (3) solid-bearing brine inclusions, and (4) high-density aqueous liquid inclusions.

The intermediate-density, two-phase inclusions (Type 1) are observed in the quartz phenocrysts and prograde skarn minerals (i.e., garnet and vesuvianite). They are up to 30 μm in diameter, commonly have negative crystal shapes but are otherwise ellipsoidal in shape; the bubble occupies 40–60 vol% of the inclusions at room temperature (20 °C; Fig. 3a–c). These fluid inclusions commonly contain one or two small opaque solids but lack halite. One of the opaque solids has a tetrahedral shape and may be chalcopyrite (Stefanini and Williams-Jones, 1996). The Type 1 inclusions in the quartz phenocrysts are irregularly distributed (Fig. 3a). In the prograde skarn, these inclusions are mainly isolated or occur as three-dimensional clusters (Fig. 3b). Some Type 1 inclusions occur along the growth zones of skarn minerals (Fig. 3c), indicating that they are primary inclusions that were trapped during the crystallization of the host minerals.

Like the Type 1 inclusions, the low-density vapor inclusions (Type 2) and brine inclusions (Type 3) are also observed in quartz phenocrysts and prograde skarn minerals. The Type 2 inclusions are up to 25 μm in diameter, contain between 65 and 90 vol% vapor and typically are dark at room temperature (Fig. 3d). Some secondary vapor inclusions were observed as trails along healed fractures (Fig. 3e). Solids were not observed in the Type 2 inclusions. Type 3 inclusions were subdivided into two types, based on the nature and the numbers of solids in them. Type 3a brine inclusions range from 15 to 25 μm in diameter, and contain halite and in some cases an opaque mineral (Fig. 3f). The consistent phase ratios among halite, liquid and vapor at room temperature indicate that the halite is a daughter mineral. Type 3b inclusions are up to 40 μm in diameter, and contain halite and up to six solids (Fig. 3g). These inclusions are only observed in the prograde skarn minerals, garnet and vesuvianite. Type 3b inclusions occur commonly as irregularly three-dimensional clusters in the garnet and are interpreted to be primary (Fig. 3g). The inconsistent phase ratios suggest that the halite was a trapped phase in Type 3b inclusions. The Type 3 inclusions are

further distinguished by their microthermometric behavior (see Section 4.2).

The high-density aqueous liquid inclusions (Type 4) occur mainly in quartz veins in the porphyry and retrograde skarn. They contain liquid and vapor, with the latter occupying between 10 and 30 vol% of an inclusion (Fig. 3h and i). Many of these inclusions are irregularly shaped. They range in diameter from 5 to 30 μm. The Type 4 inclusions occur as 3-dimensional clusters (primary) and as trails along healed fractures (secondary).

4.2. Microthermometry

Despite being cooled by liquid nitrogen to a temperature approaching −196 °C, Type 1 and 2 fluid inclusions did not freeze. This behavior is consistent with domination of the vapor by CH_4, an interpretation that was confirmed by Raman spectroscopic analyses (see below). Although the equilibrium freezing temperature of CH_4 is −182.5 °C, many studies have shown that CH_4 liquid can persist metastably to much lower temperature, i.e., below that attainable with our heating-freezing stage (Roedder, 1984, and references therein). The salinity of Type 1 and Type 2 inclusions, therefore, could not be determined from microthermometric measurements. Instead, it was determined by Raman spectroscopic analysis (see below). The salinity of the Type 3 inclusions was determined from the temperature of final dissolution of halite (Bodnar and Vityk, 1994) and that of a small number of Type 4 inclusions from the final melting temperature of CH_4-clathrate using the computer software package FLUIDS of Bakker (2003). In this study, only primary inclusions (and secondary inclusions in quartz phenocrysts) showing no evidence of post-entrapment modification were analysed microthermometrically.

Microthermometric data for the different types of fluid inclusions in the Seleteguole deposit are presented in Appendix Table 1. The Type 1 inclusions in vesuvianite homogenize at the highest temperature, namely at 413 ± 16 °C (n = 37) on average. They homogenize in quartz and garnet at a mean temperature of 390 ± 8 °C (n = 20) and 392 ± 7 °C (n = 38), respectively. Whereas the Type 1 inclusions in vesuvianite and quartz all homogenized to liquid, most of these inclusions in garnet homogenized by critical behaviour, i.e., the vapor bubble maintained a constant size upon heating until the meniscus that separates the vapor from the liquid was no longer discernible.

Homogenization of the Type 2 inclusions was difficult to observe due to their high vapor–liquid ratio and dark color. The mean homogenization temperature was 392 ± 6 °C (n = 6), 388 ± 6 °C (n = 9) and 408 ± 9 °C (n = 17) for the inclusions in quartz, garnet and vesuvianite, respectively. All these inclusions homogenized to vapor. However, three inclusions in the garnet showed near critical behavior, maintaining a constant bubble size below about 370 °C. Above this temperature, the bubble expanded rapidly and filled the entire inclusion at temperatures ≤390 °C.

The Type 3 inclusions froze at a temperature below ~−90 °C. During heating, the Type 3a inclusions homogenized either by disappearance of the vapor or complete dissolution of the halite (Appendix Table 1). Halite in the Type 3a inclusions in quartz, garnet and vesuvianite dissolved at a mean temperature of 294 ± 43 °C (n = 8), 355 ± 23 °C (n = 5) and 387 ± 32 °C (n = 7), respectively, corresponding to a salinity of 37.8 ± 3.4, 42.9 ± 2.3 and 46.1 ± 3.3 wt% NaCl equiv. Liquid–vapor homogenization of these inclusions took place at a mean temperature of 323 ± 46 °C (n = 8), 384 ± 43 °C (n = 5) and 417 ± 23 °C (n = 7), respectively. The first phase change observed upon heating of the Type 3b inclusions was the disappearance of the vapor bubble, which occurred at a mean temperature of 350 ± 6 °C (n = 3) in inclusions hosted by garnet and 382 ± 4 °C (n = 2) in inclusions hosted by vesuvianite. Most Type 3b inclusions, however, decrepitated before complete dissolution of the halite. Indeed, final homogenization was only observed for two Type 3b inclusions. In these inclusions, the vapor bubble disappeared at 343 °C and 386 °C, and complete halite dissolution occurred at 466 °C and 475 °C, respectively. The corresponding salinity was 55.1 and 56.4 wt% NaCl equiv., respectively. The highest temperature at which decrepitation occurred prior to the complete dissolution of the halite was 483 °C, corresponding to a salinity of > 57.4 wt% NaCl equiv. These microthermometric data support the conclusion from the inconsistency of the phase ratios (see above) that the halite in the Type 3b inclusions was a trapped phase.

On cooling, the Type 4 inclusions in quartz from the porphyries (veins) and skarn froze when the temperature dropped below about −40 °C. After being heated, a few of these inclusions were observed to contain clathrate which decomposed at a mean temperature of 6.8 ± 1.6 °C in porphyry (n = 3) and 7.7 ± 1.1 °C in skarn (n = 2), corresponding to a salinity of 4.2 ± 0.2 and 4.4 ± 0.2 wt% NaCl equiv., respectively. Type 4 inclusions in quartz from the porphyries (veins) and skarn homogenized at a mean temperature of 230 ± 15 °C (n = 20) and 300 ± 36 °C (n = 23), respectively.

4.3. Raman spectroscopic analysis

Raman analyses of all four types of fluid inclusion at ambient temperature yielded a peak at ~2916 cm^{-1}, showing that they contain CH_4 (Fig. 4). However, the size of CH_4 peak varied with fluid inclusion type and host mineral. The heights of the CH_4 peaks were greater for Type 1 (Fig. 4a–c) and Type 2 (Fig. 4d) inclusions than for the Type 3 (Fig. 4e) and Type 4 (Fig. 4f) inclusions in the same host (garnet). It is notable that the spectra did not contain peaks at 1285 cm^{-1} or 1388 cm^{-1}, which would have indicated the presence of CO_2. Moreover, diagnostic peaks of other gas species (e.g., H_2 at 4155 cm^{-1}) were also not observed (Fig. 4). Thus, CH_4 was the only gas species detected.

Salinity and CH_4 content were calculated from the Unsaturated Homogenized Solution Method (UHSM) of Ou et al. (2015), which makes use of the fact that when the inclusions have been homogenized to contain a single fluid phase, the Raman peak area ratios of the symmetric stretching vibrational mode of methane to the OH stretching band of water are a function of salinity and temperature (Fig. 5). As most of the Type 3 inclusions decrepitated before homogenization and homogenization of the Type 2 inclusions was difficult to observe due to their dark colour, the salinity and CH_4 content of only Type 1 and Type 4 inclusions were determined using Raman spectroscopy. These inclusions were analysed only in garnet and quartz because vesuvianite $\{Ca_{10}(Mg, Fe)Al_4[Si_2O_7]_2[SiO_4]_5(OH, F)_4\}$ contains a hydroxyl (OH) component, which produces a strong peak at the position of the water peak in the Raman spectrum (Fig. 4c). This precluded reliable calculation of the proportion of H_2O from the area under the H_2O peak.

Based on the measurements described above, the Type 1 inclusions have a mean CH_4 content of 6.5 ± 1.5 mol/kg and a mean salinity of 3.8 ± 1.3 wt% NaCl equiv (Table 1). In contrast, the mean CH_4 content of the Type 4 inclusions is only 0.8 ± 0.3 mol/kg. Their salinity is 5.4 ± 1.4 wt% NaCl equiv., which, within error, is indistinguishable from the salinity determined by clathrate decomposition (Section 4.2).

4.4. Carbon isotopes

The CH_4-bearing fluid inclusions in fourteen quartz samples from the porphyries, and five garnet and five vesuvianite samples from the skarn were analysed for their carbon isotope compositions ($\delta^{13}C_{CH4}$). The fluid inclusions in garnet, vesuvianite and vein quartz have $\delta^{13}C_{CH4}$ values ranging from −28.2‰ to −27.4‰ (PDB, average = −27.7‰), −29.4‰ to −28.5‰ (PDB, average = −28.8‰) and −29.2‰ to −19.1‰ (PDB, average = −25.5‰), respectively (Table 2). These values are similar to those of fluid inclusions in quartz from the Baogutu RPCD (from −28.6‰ to −22.6‰ with an average of −25.5‰, Cao et al., 2014).

In order to evaluate a possible relationship between the CH_4-bearing fluid and the carbonate rock hosting the skarn, the carbon isotope composition of the latter was also analyzed. Both the unaltered limestone and altered marble have uniform and positive δ^{13}Cvalues

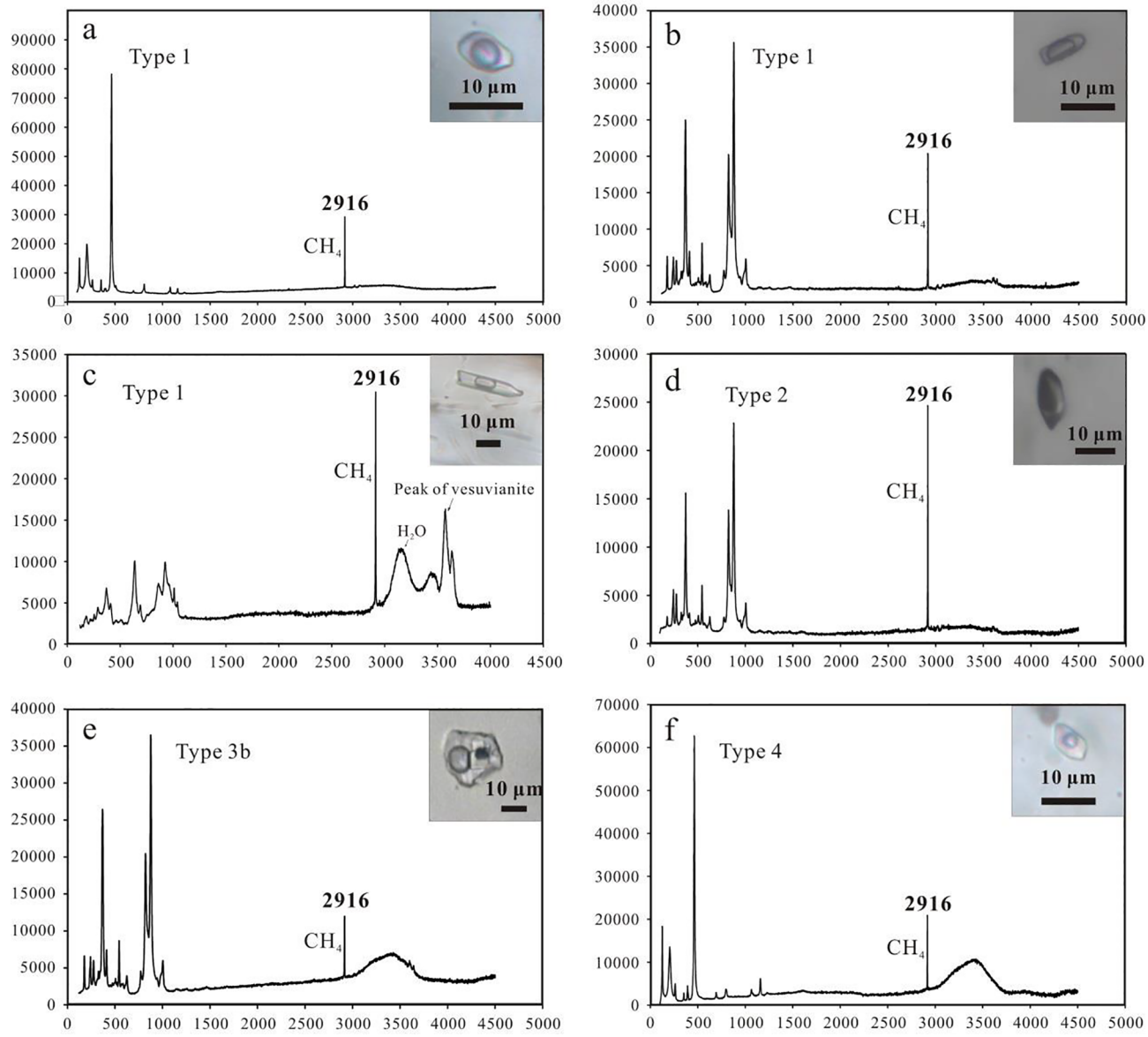

Fig. 4. Laser Raman spectra for Type 1 inclusions in quartz (a), garnet (b) and vesuvianite (c), Type 2 and Type 3b inclusions in garnet (d, e) and Type 4 inclusions in quartz veins hosted by the quartz diorite porphyry (f). The Raman peaks below 1200 cm^{-1} are attributed to the host mineral. Note the Raman peak around 3600 cm^{-1} in the vesuvianite (see text for an explanation).

between +3.9‰ and +4.4‰ (Table 3), i.e., within the range of values for marine carbonate (Rollison, 1993).

5. Discussion

5.1. Origin of the CH_4-rich fluids: epigenetic versus endogenic

The source of most components (volatiles and metals) in porphyry deposits is the magma from which they are transported by magmatic hydrothermal fluids (Hedenquist and Lowenstern, 1994). Leaching of rocks by heated circulating meteoric and ground waters, however, may also contribute components (Leybourne and Cameron, 2006; Fekete et al., 2016). Therefore, before discussing the source of CH_4-rich fluids in porphyry deposits, it is important to first determine whether the CH_4 originated from the magma (endogenic) or was incorporated into the hydrothermal system during the post-magmatic stage (epigenetic).

5.1.1. Epigenetic origin of CH_4

Reports of the occurrence of methane in magmatic–hydrothermal systems have increased during the past two decades (e.g., Potter and Konnerup-Madsen, 2003; Potter et al., 2004; Taran et al., 2010; Etiope and Sherwood Lollar, 2013). Some of the occurrences are due to the incorporation of epigenetic CH_4 during a post-magmatic stage. Methane can be incorporated into magmatic–hydrothermal fluids at subsolidus conditions through: 1) biogenic processes (Potter and Konnerup-Madsen, 2003), 2) Fischer–Tropsch synthesis (Salvi and Williams-Jones, 1997), and 3) reaction with carbonate wall rock (Etiope and Sherwood Lollar, 2013).

Biogenic CH_4 could be incorporated into a magmatic–hydrothermal fluid by bacterial activity or leaching of organic matter from the wall rocks (Gize and Macdonald, 1993; Potter and Konnerup-Madsen, 2003). Bacterial activity can be ruled out because the homogenization temperature of the CH_4-bearing fluid is well above that at which bacteria are capable of surviving. Leaching of country rocks can be also ruled out but for a different reason, in this case, because the wall rocks and their un-metamorphosed equivalents are not observed to contain organic matter. In addition, the CH_4 of biogenic origin is remarkably by the low $\delta^{13}C$ values (−110 to −30‰; Rollison, 1993; Whiticar, 1999).

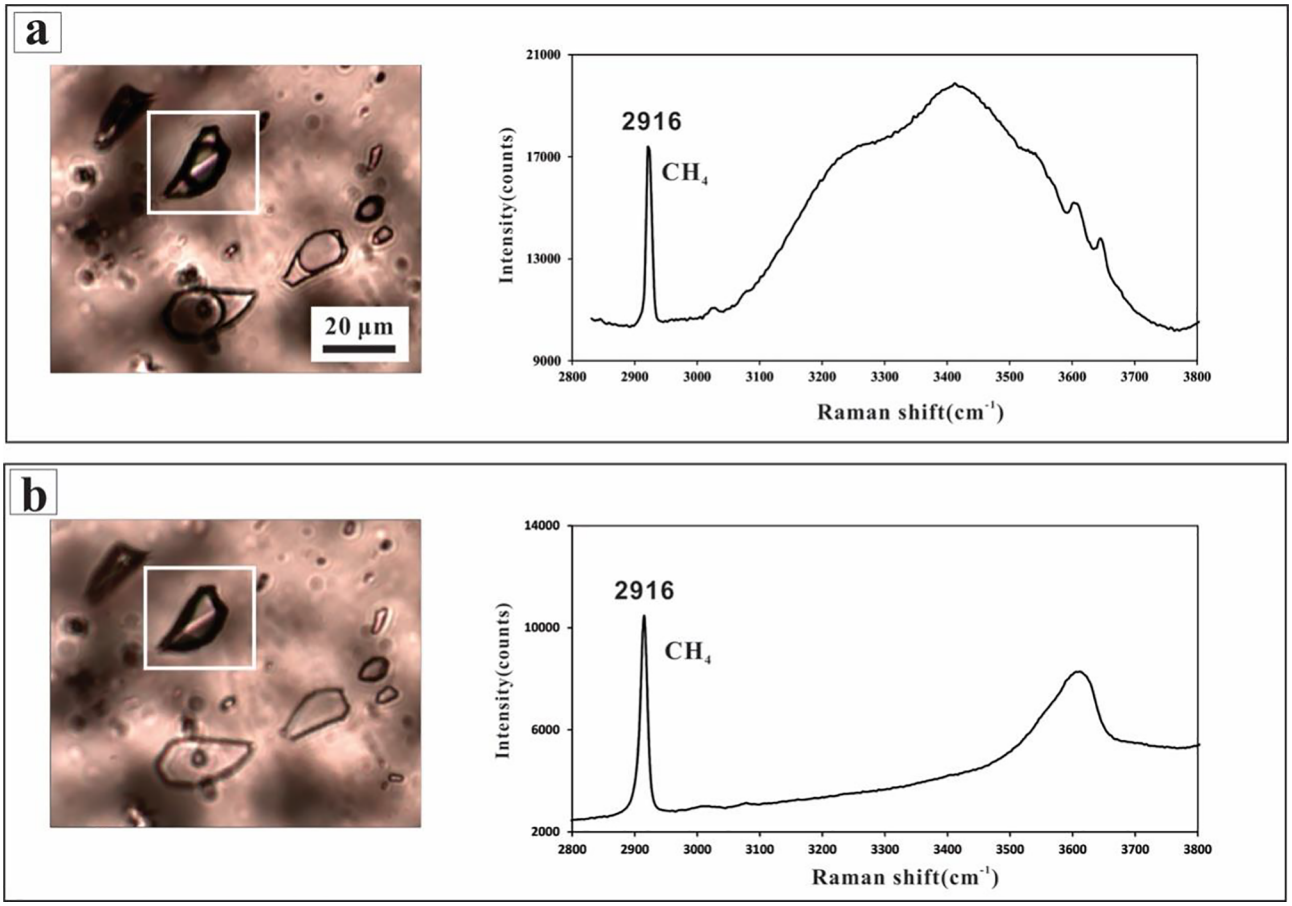

Fig. 5. Laser Raman spectra collected at room temperature (a) and the homogenization temperature (b, 400 °C) for the Type 1 inclusions.

In the case of the Seleteguole, however, the $\delta^{13}C$ values of the fluids are much higher (−29.4‰ to −19.1‰), which also eliminates the possibility that the CH_4 has a biogenic origin.

Abiogenic hydrocarbons can be generated by Fischer–Tropsch type reactions between a magmatic CO- or CO_2-dominant fluid and H_2 produced by hydrothermal reactions (Salvi and Williams-Jones, 1997; Potter et al., 2004). As mentioned in the introduction to this paper, this process was invoked by Cao et al. (2014) to interpret the widespread presence of CH_4 in the Baogutu RPCD. The Fischer–Tropsch synthesis proceeds in nature according to a reaction, catalyzed by iron or iron oxide, of the type:

$$n\ CO_2 + (3n + 1)\ H_2 \rightarrow C_nH_{2n+2} + 2n\ H_2O$$

This synthesis produces not only CH_4 (n = 1), but also other complex, higher hydrocarbons (n > 1), even at temperatures as high as 600 °C (Potter et al., 2004). Significantly, however, higher hydrocarbons are conspicuously absent from the CH_4-bearing fluid inclusions in the Seleteguole deposit (Fig. 4). Moreover, even if the synthesis was to go to completion, which will be the case if all the CO_2 or H_2 is consumed (it is unlikely that these two components would be consumed simultaneously), either CO_2 or H_2 would have been present in the inclusions. The fact that neither of these gases was detected (Fig. 4) rules out Fischer–Tropsch synthesis as a possible explanation for how the CH_4 originated.

Abiogenic methane can also be formed by the reaction of fluids with carbonate minerals under hydrothermal conditions (Horita and Berndt, 1999; Etiope and Sherwood Lollar, 2013). Indeed, this process was proposed as an alternative explanation for the presence of abundant CH_4 in the Baogutu RPCD (Shen and Pan, 2013). Furthermore, it is supported by the observation that the $\delta^{13}C$ values of the CH_4 of the Seleteguole and Baogutu deposits are similar to those predicted to result from this process (Horita and Berndt, 1999). However, CH_4 formation is prohibitively slow in the absence of catalysts (Fe or Ni metal or oxide, e.g., awaruite or magnetite) even under reducing conditions. Moreover, if catalyzed, the reaction leads to the formation of higher hydrocarbons such as C_2H_6 and C_3H_8 (Horita and Berndt, 1999; Fu et al., 2007), which are not observed at Seleteguole. Finally, if the CH_4 were sourced from a reaction with carbonate, the $\delta^{13}C$ of the reacted carbonate would have shifted towards heavier values (Horita and Berndt, 1999; Vitale Brovarone et al., 2017). However, the reacted carbonate, which at Seleteguole is represented by residual marble, has a carbon isotopic composition that is indistinguishable from that of the unreacted limestone (Fig. 6). Therefore, we conclude that the methane in the deposit could not have been produced by reaction of the fluids with the carbonate.

5.1.2. *Endogenic*

In porphyry systems, intermediate-to-felsic parent magmas commonly contain at least ca. 4 wt% H_2O (Naney, 1983; Sillitoe, 2010). When such magmas ascend to the upper crust and crystallize in response to decreasing pressure and cooling, the hydrous silicate melt becomes saturated with a volatile phase. If the volatile content is sufficient, the vapor pressure may eventually exceed the confining pressure of the system and the aqueous magmatic fluid will be exsolved from the melt (Cline and Bodnar, 1994). Such fluids are generally considered to be low-salinity, single-phase (supercritical) fluids exsolved at depths below the H_2O–NaCl solvus (Williams-Jones and Heinerich, 2005; Heinrich, 2005), resembling the high-temperature fluids captured in Type 1 inclusions at Selteguole. Commonly, these fluids have a significant carbonic component, which, given the oxidizing nature of most porphyry systems, is present as CO_2 (e.g., Redmond et al., 2004; Rusk et al., 2008; Landtwing et al., 2010; Mao et al., 2017). Under reducing conditions, such as those of RPCDs, however, this component will be present as CH_4.

A potential concern for a magmatic origin for the methane is its very

Table 1
The salinity and CH_4 content of fluid inclusions determined by quantitative Raman spectroscopic analysis.

Sample	I_{3425}	I_{3260}	I_{3425}/I_{3260}	Area (CH_4)	Area (H_2O)	PAR	T_h (K)	Manacle (mol/Kg)	Salinity (NaCl equiv. %)	mCH_4 (mol/Kg)
Type 1 inclusions										
Slt-108-01	10,473	7902	1.3254	228,179	1,060,789	0.22	673	0.56	3.17	7.44
Slt-108-02	19,466	15,095	1.2896	204,860	1,055,431	0.19	673	0.36	2.05	6.57
Slt-108-03	17,916	13,715	1.3063	233,760	1,395,015	0.17	673	0.45	2.58	5.73
Slt-108-04	6585	4873	1.3513	114,661	782,855	0.15	673	0.70	3.99	5.13
Slt-108-05	7584	5769	1.3146	172,169	921,449	0.19	673	0.50	2.84	6.42
Slt-108-06	9341	6951	1.3438	174,296	992,229	0.18	673	0.66	3.75	6.13
Slt-108-07	8095	6136	1.3193	127,492	476,784	0.27	673	0.52	2.98	9.21
Slt-108-08	5834	4288	1.3605	66,878	459,620	0.15	673	0.75	4.28	5.12
Slt-108-09	12,193	9410	1.2957	372,440	1,620,943	0.23	673	0.39	2.25	7.81
Slt-108-10	6228	4516	1.3791	149,787	903,677	0.17	673	0.85	4.86	5.88
Slt-108-11	13,196	10,092	1.3076	520,528	1,713,143	0.30	673	0.46	2.62	10.40
Slt-108-12	15,168	11,378	1.3331	165,744	798,776	0.21	673	0.60	3.42	7.20
Slt-108-13	11,384	8089	1.4073	93,234	724,446	0.13	673	1.01	5.74	4.62
Slt-108-14	3840	2808	1.3675	412,830	2,209,810	0.19	673	0.79	4.49	6.60
Slt-108-15	10,420	8026	1.2983	91,748	833,870	0.11	673	0.41	2.33	3.75
Slt-108-16	3564	2495	1.4285	135,659	782,827	0.17	673	1.12	6.40	6.28
Slt-108-17	5945	4200	1.4155	170,011	936,977	0.18	673	1.05	5.99	6.54
Slt-108-18	2858	2055	1.3908	214,938	1,083,291	0.20	673	0.92	5.22	7.08
Slt-108-19	2141	1584	1.3516	229,175	1,536,766	0.15	673	0.70	4.00	5.22
Type 4 inclusions										
Slt-3-01	5817	4246	1.3700	43,197	1,617,564	0.027	573	0.80	4.57	1.05
Slt-3-02	13,606	9930	1.3702					0.80	4.58	
Slt-3-03	17,152	12,181	1.4081	12,263	748,932	0.016	573	1.01	5.76	0.65
Slt-3-04	17,571	13,323	1.3188	17,956	2,201,869	0.008	573	0.52	2.97	0.31
Slt-3-05	24,706	17,518	1.4103	62,685	3,079,831	0.020	573	1.02	5.83	0.81
Slt-3-06	12,093	8428	1.4349					1.16	6.60	
Slt-3-07	18,696	12,816	1.4588	100,545	3,202,540	0.031	573	1.29	7.34	1.27

I_{3425} and I_{3260} are signal intensities at 3425 cm^{-1} and 3260 cm^{-1} (at room temperature).
The areas of the Raman peaks for CH_4 (Area CH_4) and H_2O (Area H_2O) were obtained using the software GRAMS/AI (Thermo Galactic).
PAR is the Raman peak area ratio of CH_4 and H_2O at the homogenization temperature.
T_h is the homogenization temperature in K.
$mNaCl = -0.116\ (I_{3425}/I_{3260})^2 + 5.805\ (I_{3425}/I_{3260}) - 6.933$.
$mCH4 = PAR/QF$, $QF = (-1.001E-05 \times mNaCl^{1/2} + 3.703E-05)T + (2.546E-03 \times mNaCl^{1/2} + 7.128E-03)$.

Table 2
The carbon isotope composition of the CH_4 in the fluid inclusions.

Sample	Host mineral	$\delta^{13}C_{V\text{-}PDB}$ (‰)
SLT-2-1	Quartz	−27.6
SLT-2-2	Quartz	−27.5
SLT-2-3	Quartz	−27.4
SLT-3-1	Quartz	−26.3
SLT-3-2	Quartz	−25.8
SLT-3-3	Quartz	−27.0
SLT-5-1	Quartz	−29.2
SLT-5-2	Quartz	−24.8
SLT-5-3	Quartz	−27.1
SLT-8-1	Quartz	−27.9
SLT-8-2	Quartz	−26.9
SLT-27-1	Quartz	−20.5
SLT-33-1	Quartz	−19.1
SLT-33-2	Quartz	−19.2
SLT-14-1	Garnet	−27.4
SLT-14-2	Garnet	−27.6
SLT-35-1	Garnet	−27.7
SLT-35-2	Garnet	−27.4
SLT-56-1	Garnet	−28.2
SLT-20-1	Vesuvianite	−29.4
SLT-20-2	Vesuvianite	−28.7
SLT-78-1	Vesuvianite	−28.5
SLT-104-2	Vesuvianite	−28.8
SLT-104-3	Vesuvianite	−28.5

high content in Type 1 inclusions (3.3–7.4 mol/kg). This concern, however, is easily met by the observation that methane is completely miscible in water at supercritical conditions, although its solubility decreases sharply with decreasing temperature below the critical point (Lamb et al., 1996; Krader and Franck, 1987). At the conditions of entrapment of the Type 1 inclusions (> 400 °C), the solubility of CH_4 in the hydrothermal fluid is, therefore, likely to have been very high.

Given the very high CH_4 contents of the Type 1 inclusions it is also necessary to consider whether granitoid magmas can dissolve sufficient CH_4. There is direct evidence from some melt and fluid inclusion studies that CH_4-dominant fluids can coexist with magma, e.g., the recent study of Vasyukova et al. (2016) documenting the coexistence of melt and CH_4 inclusions in a granite pluton. This conclusion is also supported by the occurrences of CH_4 bearing melt inclusions in silicate rocks (Li and Chou, 2014; Wang et al., 2014; Liu et al., 2015). We, therefore, conclude that the CH_4 in the Seleteguole ore-forming system was part of the hydrothermal fluid that exsolved from the magma which gave rise to the syn-mineralization diorite porphyry and quartz diorite porphyry intrusions.

5.2. Potential reservoirs for CH_4

Chemically, the granitoids in the vicinity of the Seleteguole deposit show evidence of having crystallized in an arc environment, indicating that the corresponding magmas were generated during subduction (Zhang et al., 2016). Their positive mantle-like zircon $\varepsilon_{Hf}(t)$ values (+6.6 to +11.3) also show that the magmas did not experience significant crustal contamination during their ascent and emplacement (Zhang et al., 2016). We therefore conclude that the CH_4 must have been introduced in the subduction zone.

There are three main sources for abiotic CH_4 of magmatic origin in subduction zones: 1) re-speciation of C–O–H fluids during magma cooling (Potter and Konnerup-Madsen, 2003); 2) deep reduced asthenospheric mantle (Liu and Fei, 2006; Cao et al., 2016); and 3) high-pressure methanogenesis in the subduction zone (Tao et al., 2018;

Table 3
The carbon isotope composition of the limestone and marble in the Seleteguole deposit.

Sample	Lithology	$\delta^{13}C_{V\text{-}PDB}$ (‰)
SLT-62-1	Limestone	4.31
SLT-62-2	Limestone	4.35
SLT-62-3	Limestone	4.35
SLT-63-1	Limestone	4.28
SLT-63-2	Limestone	4.38
SLT-63-3	Limestone	4.36
SLT-62-4	Marble	3.90
SLT-62-5	Marble	3.92
SLT-62-6	Marble	3.93
SLT-64-1	Marble	3.87
SLT-64-2	Marble	3.88
SLT-69-1	Marble	3.86

Vitale Brovarone et al., 2017). In the following sub-sections, we evaluate the potential contributions of these sources to the CH_4 budget of the Seleteguole ore-forming system.

5.2.1. Respeciation of C–O–H fluid during magma cooling

During magma cooling, a CH_4-rich fluid can evolve in a closed system from re-equilibration of a magmatic CO_2–H_2O fluid at low oxygen fugacity, i.e., ≤QFM – 2 (Potter and Konnerup-Madsen, 2003; Etiope and Sherwood Lollar, 2013), and this process has been used to explain the presence of CH_4 in some magmatic systems (e.g., Gerlach, 1980; Kogarko et al., 1987; Konnerup-Madsen, 2001). However, re-speciation of C–O–H to form CH_4 requires low temperature (< 500 °C) and, thus, is restricted to magmas with very low solidus temperatures (Potter and Konnerup-Madsen, 2003). At Seleteguole, the related magma had a dioritic composition, and such magmas have solidus temperatures on the order of 850 °C (Ebadi and Johannes, 1991). It therefore follows that the Seleteguole diorite could not have provided a favorable environment for CH_4 formation through C–O–H respeciation.

5.2.2. Reduced asthenospheric mantle

Although many studies have concluded that CO_2 and H_2O are the major fluid species in the upper mantle (Roedder, 1965; Ertan and Leeman, 1999), some researchers have proposed that the deeper asthenospheric mantle may contain primordial CH_4 and other hydrocarbons (e.g., Gold, 1979; Giardini et al., 1982) and that these hydrocarbons may migrate into the upper mantle through a slab window (e.g., Cao et al., 2016). However, the $\delta^{13}C$ values of CH_4 in the Seleteguole and Baogutu deposits (from −29.2‰ to −19.1‰ and from −28.6‰ to −22.6‰, respectively) are too negative to be of asthenospheric mantle origin ($\delta^{13}C = -5 \pm 2$‰; Deines, 2002), indicating that the CH_4 in these RPCDs could not have been sourced directly from the asthenospheric mantle.

5.2.3. Methanogenesis in the subduction zone

Methanogenesis ocurrs mainly at low temperature and pressure and shallow depth (Etiope and Sherwood Lollar, 2013). However, methane has also been shown experimentally to form and be stable at high temperature and pressure (Scott et al., 2004; Chen et al., 2008; Kolesnikov et al., 2009). Thus, an obvious environment in which such abiotic methane might be produced is subducted oceanic slab, which contains carbonate and ultramafic rocks with high reducing potential (Vitale Brovarone et al., 2017) and, indeed, this is the case as shown by the occurrence of CH_4-bearing fluid inclusions in metamorphic rocks from subduction zones (Fu et al., 2003; Shi et al., 2005; Arai et al., 2012; Vitale Brovarone et al., 2017). Significantly, for our study, abundant CH_4 inclusions also have been recently detected in the ultra-high pressure subduction-related metamorphic rocks of the western Tianshan (Tao et al., 2018). According to Tao et al. (2018), the oxygen fugacity of western Tianshan subduction zone is relatively low (FMQ – 2.5) and reduced CH4-bearing fluid is continually released from subducting slab to the overlying mantle wedge.

We can test the applicability of the subduction-related methanogenetic model using carbon isotopes. Assuming that the source of the CH_4 was slab-derived carbonate rocks (see Tao et al., 2018), and that they comprised a mixture of carbonate ($\delta^{13}C \approx 0$‰) and organic matter ($\delta^{13}C \approx -27$‰). Based on carbon isotopic fractionation equation of Horita (2001), formation of the Seleteguole reduced fluid (−29.2 to −19.1‰) require reduction of carbonate combined with 37.8–75.2% of organic materials at the temperature of 600 °C. The produced CH_4 at subduction zone could be dissolved in the arc magma and ascended to the upper regions of the crust. We also note that this hypothesis is supported by the presence of CH_4-rich fluid inclusions in some mafic–ultramafic intrusions (~280 Ma; Liu and Fei, 2006) located close to

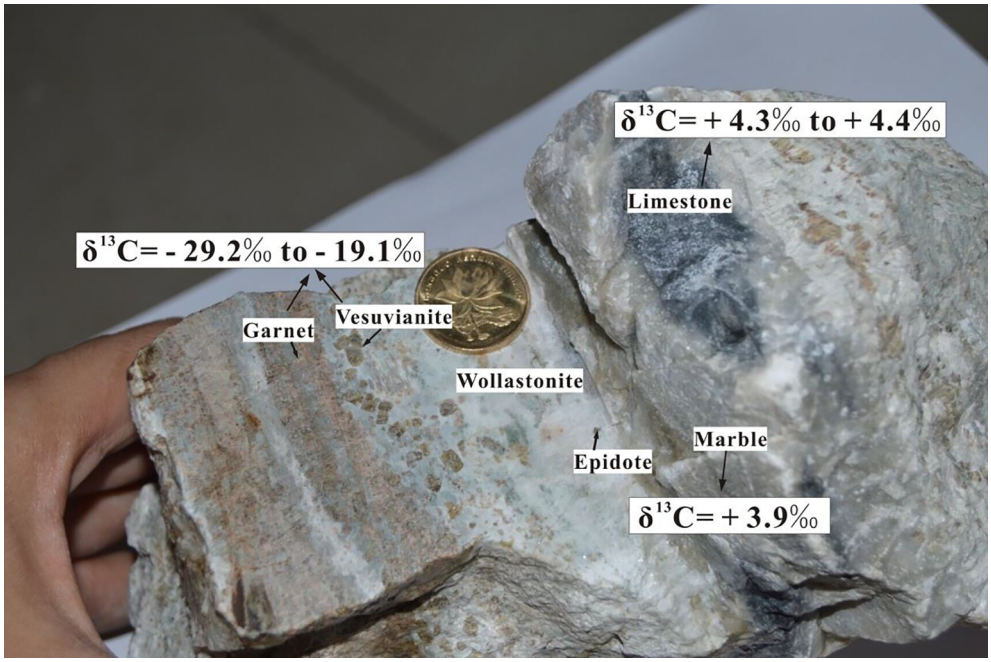

Fig. 6. A hand sample from the Seleteguole deposit, illustrating the transition from limestone/marble to skarn. Carbon isotope compositions for the CH_4 in the fluid inclusions, limestone and marble are also shown.

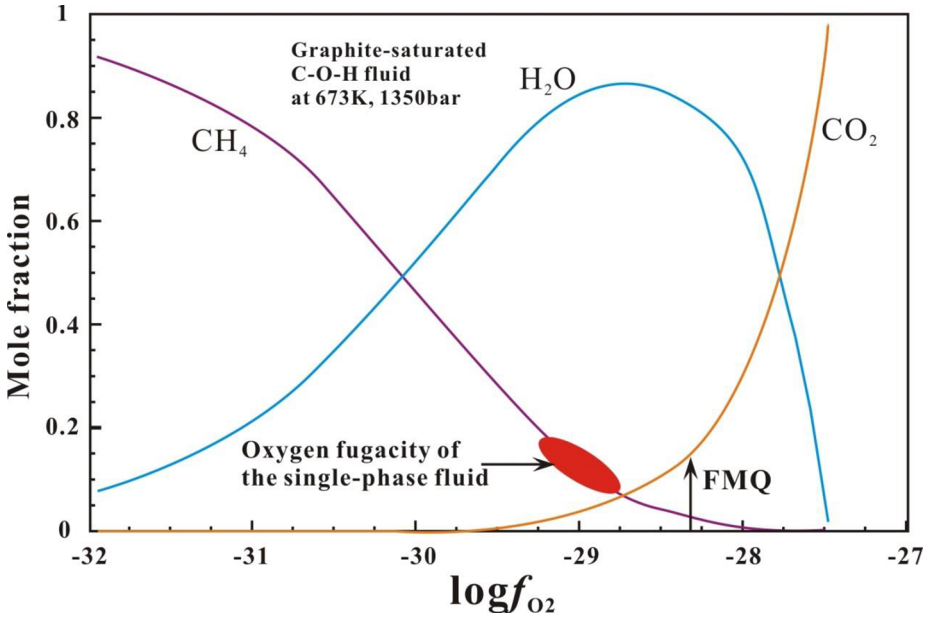

Fig. 7. Mole fractions of the species in graphite-saturated C–O–H fluids as a function of oxygen fugacity at 673 K, 1350 bar (H_2 and CO were not considered). The red domain represents the oxygen fugacity (ΔFMQ − 1 to ΔFMQ − 0.5) of the Type 1 fluid inclusions in the Seleteguole deposit. The mole fractions of CO_2, CH_4 and H_2O at various oxygen fugacities were calculated using the GFluid program of Zhang and Duan (2010). (For interpretation of the references to color in this figure legend, the reader is referred to the web version of this article.)

the Seleteguole deposit.

To summarize, reduction of carbanate rocks in a subduction zone is the most plausible hypothesis to explain the occurrence of CH_4 in the Seleteguole RPCD. Our study not only suggests that abiotic methanogenesis in the subduction zone may be a more common process than previously thought but also implies that CH_4 is readily dissolved in arc magmas, which transport it to shallow depth.

5.3. Ore metal transport in reduced fluids

The ore-forming fluids in porphyry systems are generally oxidized, with the oxygen fugacity (fO_2) being typically two orders of magnitude above the fayalite–magnetite–quartz oxygen buffer (ΔFMQ + 2) (e.g., Mungall, 2002; Sun et al., 2013). The presence of CH_4 in primary fluid inclusions at Seleteguole, however, indicates that the fluids responsible for forming this deposit were reduced. Indeed, based on the mole fraction of CH_4 in these inclusions and the distribution of species in the C–O–H system at 400 °C and 1350 bar (assuming the Type 1 inclusions were trapped at 5 km depth), we estimate that the oxygen fugacity was between 0.5 and 1 log unit below FMQ (Fig. 7).

Numerous studies have emphasized the importance of bisulfide complexes (HS^-) in transporting metals, especially under reducing conditions (e.g., Crerar and Barnes, 1976; Mountain and Seward, 2003; Seo et al., 2009). However, experimental speciation studies reviewed in Williams-Jones and Migdisov (2014) show that for the salinity and temperature typically encountered in porphyry systems, Cu is transported dominantly as an aqueous chloride complex (e.g., $CuCl_2^-$), even under relatively reducing conditions; Mo is transported dominantly as oxoyacid species (e.g., MoO_4^{2-}, MoO_3^{2-}). According to Williams-Jones and Migdisov (2014), both Cu and Mo have higher solubility in oxidized fluids (liquids) than in reduced fluids but the difference decreases with increasing temperature. In the temperature range from 450 to 560 °C, the solubility of Cu in a fluid buffered by the assemblage pyrite–magnetite–hematite (oxidized) is 400–2300 ppm, whereas in a fluid buffered by the assemblage pyrite–pyrrhotite–magnetite (reduced) it is 250–2000 ppm. The lower solubility of Cu and Mo in reduced fluids may be the reason that the currently known RPCDs are generally small- to medium-sized. Another reason probably result in the small size of RPCDs is that a significant portion of Cu will partition into sulfide phases in reduced silicate melt and precipitated before transported to the surface (Sun et al., 2013). Based on the Hard/Soft Acid/Base principle of Pearson (1963), Au+ is soft metal and will bond preferentially with soft bases (ligands), i.e., HS^- in the fluid. Therefore, in contrast to Cu, Au is likely to be transported in hydrothermal fluids under reducing conditions dominantly as complexes involving HS^-. Significantly, most of the World's RPCDs, including Seleteguole, are Au-rich (e.g., Rowins, 2000; Smith et al., 2012; Cao et al., 2014), which is consistent with the observation that, in contrast to Cu, which is transported dominantly as a chloride complex, Au transport as a bisulfide complex is actually promoted by relatively reducing conditions (Williams-Jones and Migdisov, 2014).

6. Concluding remarks

The results of this study show that the ore fluids in the Seleteguole porphyry–skarn Cu–Mo–Au deposit were exsolved directly from a dioritic magma. The very high CH_4 content (3.8–10.4 mol/kg) of these fluids, corresponding to an oxygen fugacity of between ΔFMQ − 0.5 and ΔFMQ − 1, indicates that the magmas and fluids at Seleteguole were reduced. This contrasts with the finding that most porphyry deposits originate from relatively oxidizing magmas (ΔFMQ + 2) and can be explained by invoking organic rich, carbonate rock-mediated methanogenesis in the subduction zone. The reduced magmatic CH_4-rich fluids are interpreted to have carried the metal required to form the deposit. Although the solubility of Cu and Mo is lower in reducing fluids than in oxidizing fluids, the difference is not significant. Moreover, Au solubility is actually enhanced in reducing fluids, potentially explaining why the Seleteguole deposit and other RPCD deposits are enriched in Au.

Acknowledgements

This research was jointly supported by the National Key R&D Program of China (2016YFC0600305), the Chinese NSF Projects (41872097, 41673051). Jia-Li Cai, Wan-Jun Lu, Ya-Hao Huang and Han-Bin Liu are thanked for their assistance in laboratory analyses. Qiu-Yue Huang and Li Zhou helped to improve this manuscript. We are grateful to the two official reviews and editorial handling by Franco Pirajno and Mei Yuan.

Appendix A

See Table 1.

Table 1
Microthermometric results of fluid inclusion in the Seleteguole deposit.

Inclusion type	Sample type	Size (μm)	Bubble volume range (vol%)	Clathrate melting temperature	Halite melting temperature	Homogenization temperature range	Mode of homogenization	Salinity (wt % NaCl equiv.)
Intermediate-density inclusions (Type 1)	Quartz	20 × 15	50			387	Liquid	
	Quartz	25 × 18	50			385	Liquid	
	Quartz	20 × 15	50			389	Liquid	
	Quartz	15 × 12	45			392	Liquid	
	Quartz	18 × 10	45			380	Liquid	
	Quartz	20 × 12	50			388	Liquid	
	Quartz	10 × 5	50			396	Liquid	
	Quartz	12 × 10	50			371	Liquid	
	Quartz	15 × 12	50			405	Liquid	
	Quartz	13 × 9	50			399	Liquid	
	Quartz	10 × 8	45			380	Liquid	
	Quartz	12 × 9	50			388	Liquid	
	Quartz	12 × 10	45			392	Liquid	
	Quartz	10 × 5	40			391	Liquid	
	Quartz	10 × 7	40			401	Liquid	
	Quartz	25 × 15	40			399	Liquid	
	Quartz	20 × 14	50			398	Liquid	
	Quartz	15 × 10	50			399	Liquid	
	Quartz	18 × 12	45			389	Liquid	
	Quartz	15 × 10	45			381	Liquid	
	Garnet	25 × 10	60			405	Critical behavior	
	Garnet	15 × 7	60			388	Critical behavior	
	Garnet	18 × 9	60			391	Critical behavior	
	Garnet	12 × 6	55			387	Critical behavior	
	Garnet	20 × 10	60			390	Critical behavior	
	Garnet	14 × 8	60			385	Critical behavior	
	Garnet	16 × 8	55			392	Critical behavior	
	Garnet	25 × 12	55			386	Critical behavior	
	Garnet	32 × 20	55			391	Critical behavior	
	Garnet	30 × 20	50			388	Critical behavior	
	Garnet	10 × 6	55			392	Critical behavior	
	Garnet	15 × 8	50			395	Critical behavior	
	Garnet	17 × 8	50			391	Critical behavior	
	Garnet	13 × 7	50			398	Critical behavior	
	Garnet	13 × 7	50			391	Critical behavior	
	Garnet	10 × 5	60			402	homogenization to liquid	
	Garnet	22 × 10	60			400	homogenization to liquid	
	Garnet	25 × 12	60			400	homogenization to liquid	
	Garnet	23 × 15	60			396	Critical behavior	
	Garnet	17 × 12	50			395	Critical behavior	
	Garnet	18 × 10	50			392	Critical behavior	
	Garnet	17 × 8	50			393	Critical behavior	
	Garnet	10 × 6	55			400	Critical behavior	
	Garnet	8 × 5	55			396	Critical behavior	
	Garnet	10 × 5	55			382	Critical behavior	
	Garnet	16 × 12	60			395	homogenization to liquid	
	Garnet	23 × 12	55			396	homogenization to liquid	
	Garnet	26 × 14	55			385	Critical behavior	
	Garnet	20 × 10	50			384	Critical behavior	
	Garnet	22 × 10	55			408	Critical behavior	
	Garnet	16 × 10	50			388	Critical behavior	

(*continued on next page*)

Table 1 (*continued*)

Inclusion type	Sample type	Size (μm)	Bubble volume range (vol%)	Clathrate melting temperature	Halite melting temperature	Homogenization temperature range	Mode of homogenization	Salinity (wt % NaCl equiv.)
	Garnet	19 × 10	50			385	Critical behavior	
	Garnet	17 × 9	50			382	Critical behavior	
	Garnet	18 × 8	50			385	Critical behavior	
	Garnet	26 × 14	55			388	Critical behavior	
	Garnet	27 × 13	55			380	Critical behavior	
	Garnet	25 × 10	55			385	Critical behavior	
	Garnet	19 × 10	50			390	Critical behavior	
	Vesuvianite	20 × 10	55			388	Liquid	
	Vesuvianite	22 × 10	55			400	Liquid	
	Vesuvianite	18 × 12	55			396	Liquid	
	Vesuvianite	15 × 12	55			404	Liquid	
	Vesuvianite	16 × 8	55			397	Liquid	
	Vesuvianite	17 × 8	55			396	Liquid	
	Vesuvianite	25 × 4 (elongated)	60			413	Liquid	
	Vesuvianite	30 × 4 (elongated)	60			430	Liquid	
	Vesuvianite	25 × 4 (elongated)	60			428	Liquid	
	Vesuvianite	20 × 4 (elongated)	60			427	Liquid	
	Vesuvianite	50 × 4 (elongated)	60			405	Liquid	
	Vesuvianite	25 × 4 (elongated)	60			442	Liquid	
	Vesuvianite	28 × 4 (elongated)	60			405	Liquid	
	Vesuvianite	18 × 8	50			389	Liquid	
	Vesuvianite	20 × 9	55			426	Liquid	
	Vesuvianite	35 × 5 (elongated)	55			430	Liquid	
	Vesuvianite	19 × 10	50			398	Liquid	
	Vesuvianite	20 × 8	55			416	Liquid	
	Vesuvianite	22 × 10	55			416	Liquid	
	Vesuvianite	23 × 10	55			411	Liquid	
	Vesuvianite	35 × 5 (elongated)	60			454	Liquid	
	Vesuvianite	25 × 5(elongated)	60			408	Liquid	
	Vesuvianite	30 × 5 (elongated)	60			430	Liquid	
	Vesuvianite	25 × 5 (elongated)	60			421	Liquid	
	Vesuvianite	40 × 5 (elongated)	60			450	Liquid	
	Vesuvianite	20 × 5 (elongated)	60			405	Liquid	
	Vesuvianite	25 × 5 (elongated)	60			406	Liquid	
	Vesuvianite	20 × 9	50			412	Liquid	
	Vesuvianite	18 × 8	50			410	Liquid	
	Vesuvianite	22 × 10	50			395	Liquid	
	Vesuvianite	17 × 9	50			409	Liquid	
	Vesuvianite	20 × 10	50			397	Liquid	
	Vesuvianite	25 × 5 (elongated)	60			418	Liquid	
	Vesuvianite	35 × 5 (elongated)	60			435	Liquid	
	Vesuvianite	22 × 5 (elongated)	60			406	Liquid	
	Vesuvianite	15 × 10	55			397	Liquid	
	Vesuvianite	18 × 12	55			407	Liquid	
Low-density vapor inclusions (Type 2)	Quartz	16 × 15	70			378	Vapor	
	Quartz	15 × 12	65			386	Vapor	
	Quartz	14 × 12	70			390	Vapor	
	Quartz	10 × 8	70			392	Vapor	
	Quartz	20 × 16	80			386	Vapor	
	Quartz	18 × 15	75			392	Vapor	
	Garnet	12 × 9	85			377	Vapor	
	Garnet	14 × 10	75			388	Near critical behavior	

(*continued on next page*)

Table 1 (*continued*)

Inclusion type	Sample type	Size (μm)	Bubble volume range (vol%)	Clathrate melting temperature	Halite melting temperature	Homogenization temperature range	Mode of homogenization	Salinity (wt % NaCl equiv.)
	Garnet	12 × 10	75			388	Near critical behavior	
	Garnet	20 × 15	80			387	Near critical behavior	
	Garnet	23 × 20	85			379	Vapor	
	Garnet	25 × 20	80			394	Vapor	
	Garnet	22 × 18	75			396	Vapor	
	Garnet	15 × 13	75			392	Vapor	
	Garnet	16 × 15	80			397	Vapor	
	Garnet	15 × 13	85			403	Vapor	
	Garnet	13 × 12	90			388	Vapor	
	Vesuvianite	15 × 12	80			407	Vapor	
	Vesuvianite	13 × 12	75			406	Vapor	
	Vesuvianite	12 × 10	75			410	Vapor	
	Vesuvianite	17 × 15	75			407	Vapor	
	Vesuvianite	18 × 15	80			407	Vapor	
	Vesuvianite	10 × 8	85			411	Vapor	
	Vesuvianite	15 × 12	85			401	Vapor	
	Vesuvianite	13 × 10	85			399	Vapor	
	Vesuvianite	14 × 12	80			398	Vapor	
	Vesuvianite	20 × 15	80			410	Vapor	
	Vesuvianite	13 × 12	75			399	Vapor	
	Vesuvianite	14 × 13	75			397	Vapor	
	Vesuvianite	15 × 13	75			396	Vapor	
	Vesuvianite	16 × 15	80			405	Vapor	
	Vesuvianite	17 × 15	80			415	Vapor	
	Vesuvianite	15 × 13	75			407	Vapor	
Type 3a brine inclusions	Quartz	20 × 15	20		307	385	Liquid	38.7
	Quartz	18 × 14	20		288	374	Liquid	37.2
	Quartz	17 × 12	30		285	268	Liquid	36.9
	Quartz	20 × 16	30		210	277	Liquid	32.4
	Quartz	20 × 16	30		256	310	Liquid	35
	Quartz	15 × 12	25		328	276	Liquid	40.5
	Quartz	15 × 12	25		364	319	Liquid	43.8
	Quartz	17 × 15	20		311	377	Liquid	40
	Garnet	15 × 8	25		410	354	Liquid	48.5
	Garnet	20 × 10	25		346	383	Liquid	42.1
	Garnet	25 × 12	25		387	320	Liquid	45.9
	Garnet	18 × 9	30		367	430 decrepitated	Liquid	44
	Garnet	18 × 8	30		355	432	Liquid	42.9
	Vesuvianite	23 × 12	30		426 decrepitated	410	Liquid	50.2
	Vesuvianite	18 × 10	30		375	453 decrepitated	Liquid	44.8
	Vesuvianite	20 × 8	30		372	398	Liquid	44.5
	Vesuvianite	15 × 8	30		371	428	Liquid	44.4
	Vesuvianite	20 × 10	30		421	438 decrepitated	Liquid	49.8
	Vesuvianite	17 × 8	25		330	415	Liquid	40.6
	Vesuvianite	20 × 12	25		411	378	Liquid	48.6
Type 3b brine inclusions	Garnet	25 × 20	15		464 decrepitated	357	Liquid	55.1
	Garnet	18 × 10	20		467 decrepitated	350	Liquid	55.1
	Garnet	30 × 25	10		466	343	Liquid	56.2
	Vesuvianite	22 × 18	15		475	386	Liquid	56.3

(*continued on next page*)

Table 1 (*continued*)

Inclusion type	Sample type	Size (μm)	Bubble volume range (vol%)	Clathrate melting temperature	Halite melting temperature	Homogenization temperature range	Mode of homogenization	Salinity (wt % NaCl equiv.)
	Vesuvianite	25 × 20	15		483 decrepitated	378	Liquid	57.4
Aqueous liquid inclusions (Type 4)	Quartz veins in porphyry	15 × 12	20			220	Liquid	
	Quartz veins in porphyry	20 × 12	20			231	Liquid	
	Quartz veins in porphyry	17 × 12	20			230	Liquid	
	Quartz veins in porphyry	15 × 10	25			234	Liquid	
	Quartz veins in porphyry	12 × 8	25	7.3		232	Liquid	4.2
	Quartz veins in porphyry	10 × 5	25			214	Liquid	
	Quartz veins in porphyry	10 × 6	15			228	Liquid	
	Quartz veins in porphyry	13 × 8	15			221	Liquid	
	Quartz veins in porphyry	12 × 9	15			228	Liquid	
	Quartz veins in porphyry	20 × 15	25			223	Liquid	
	Quartz veins in porphyry	20 × 15	25			212	Liquid	
	Quartz veins in porphyry	22 × 18	25			218	Liquid	
	Quartz veins in porphyry	25 × 18	25			253	Liquid	
	Quartz veins in porphyry	25 × 20	30	4.6		269	Liquid	8.1
	Quartz veins in porphyry	20 × 10	25			222	Liquid	
	Quartz veins in porphyry	16 × 12	25			220	Liquid	
	Quartz veins in porphyry	20 × 15	25	8.4		235	Liquid	4.3
	Quartz veins in porphyry	14 × 10	20			245	Liquid	
	Quartz veins in porphyry	15 × 10	20			215	Liquid	
	Quartz veins in porphyry	12 × 8	25			228	Liquid	
	Quartz veins in porphyry	13 × 8	25			225	Liquid	
	Quartz veins in porphyry	15 × 12	25			261	Liquid	
	Quartz veins in skarn	15 × 12	20			285	Liquid	
	Quartz veins in skarn	16 × 8	20			275	Liquid	
	Quartz veins in skarn	18 × 10	20			283	Liquid	
	Quartz veins in skarn	15 × 12	20			305	Liquid	
	Quartz veins in skarn	15 × 10	15			273	Liquid	
	Quartz veins in skarn	20 × 15	15			320	Liquid	
	Quartz veins in skarn	22 × 15	30			341	Liquid	
	Quartz veins in skarn	20 × 10	25	8.7		304	Liquid	4.3
	Quartz veins in skarn	15 × 8	30			350	Liquid	
	Quartz veins in skarn	10 × 6	20			337	Liquid	
	Quartz veins in skarn	17 × 10	25			314	Liquid	
	Quartz veins in skarn	22 × 15	25			255	Liquid	
	Quartz veins in skarn	30 × 25	25	6.6		310	Liquid	5.1
	Quartz veins in skarn	18 × 12	25			305	Liquid	
	Quartz veins in skarn	25 × 20	30			318	Liquid	
	Quartz veins in skarn	17 × 10	25			290	Liquid	
	Quartz veins in skarn	18 × 10	25			324	Liquid	
	Quartz veins in skarn	15 × 10	20			333	Liquid	
	Quartz veins in skarn	22 × 12	20			306	Liquid	

Appendix B. Supplementary data

Supplementary data to this article can be found online at https://doi.org/10.1016/j.oregeorev.2019.103135.

References

Arai, S., Ishimaru, S., Mizukami, T., 2012. Methane and propane micro-inclusions in olivine in titanoclinohumite-bearing dunites from the Sanbagawa high-P metamorphic belt, Japan: hydrocarbon activity in a subduction zone and Ti mobility. Earth Planet. Sci. Lett. 353–354, 1–11.

Bakker, R.J., 2003. Package FLUIDS 1. Computer programs for analysis of fluid in clusion data and for modlling bulk fluid properties. Chem. Geol. 194, 3–23.

Bodnar, R.J., Vityk, M.O., 1994. Interpretation of microthermometric data for H_2O-NaCl fluid inclusions. In: de Vivo, B., Frezzotti, M.L. (Eds.), Fluid Inclusions in Quartz at One Atmosphere Confining Pressure. J. Metamorph. Geol. pp. 229–242.

Cao, M.J., Qin, K.Z., Li, G.M., Evans, N.J., Jin, L.Y., 2014. Abiogenic Fischer-Tropsch synthesis of methane at the Baogutu reduced porphyry copper deposit, western Junggar, NW-China. Geochim. Cosmochim. Acta 141, 179–198.

Cao, M.J., Qin, K.Z., Li, G.M., Evans, N.J., Hollings, P., Jin, L.Y., 2016. Genesis of ilmenite-series I-type granitoids at the Baogutu reduced porphyry Cu deposit, western Junggar, NW-China. Lithos 246–247, 13–30.

Chen, J.Y., Jin, L.J., Dong, J.P., Zheng, H.F., Liu, G.Y., 2008. Methane formation from $CaCO_3$ reduction catalyzed by high pressure. Chin. Chem. Lett. 19, 475–478.

Cline, J.S., Bodnar, R.J., 1994. Dircet evolution of brine from a crystallizing silicic melt at the Questa, New Mexico, molybdenum deposit. Econ. Geol. 89, 1780–1802.

Crerar, D.A., Barnes, H.L., 1976. Ore solution chemistry, V: solubilities of chalcopyrite and chalcocite assemblage in hydrothermal solution at 200°C to 350°C. Econ. Geol. 71, 772–794.

Deines, P., 2002. The carbon isotope geochemistry of mantle xenoliths. Earth-Sci. Rev. 58, 247–278.

Dubessy, J., Buschaert, S., Lamb, W., Pironon, J., Thiéry, R., 2001. Methane-bearing aqueous fluid inclusions: Raman analysis, thermodynamic modelling and application to petroleum basins. Chem. Geol. 173, 193–205.

Ebadi, A., Johannes, W., 1991. Beginning of melting and composition of first melts in the system Qz-Ab-Or-H_2O-CO_2. Contrib. Mineral. Petrol. 106, 286–295.

Ertan, I.E., Leeman, W.P., 1999. Fluid inclusions in mantle and lower crustal xenoliths from the Simcoe volcanic field, Washington. Chem. Geol. 154, 83–95.

Etiope, G., Sherwood Lollar, B., 2013. Abiotic methane on earth. Rev. Geophys. 51, 276–299.

Fekete, S., Weis, P., Driesner, T., Bouvier, A.S., Baumgartner, L., Heinrich, C.A., 2016. Contrasting hydrological processes of meteoric water incursion during magmatic–hydrothermal ore deposition: an oxygen isotope study by ion microprobe. Earth Planet. Sci. Lett. 451, 263–271.

Fiebig, J., Woodland, A.B., Spangenberg, J., Oschmann, W., 2007. Natural evidence for rapid abiogenic hydrothermal generation of CH_4. Geochim. Cosmochim. Acta 71, 3028–3039.

Fu, Q., Sherwood Lollar, B., Horita, J., Lacrampe-Couloume, G., Seyfried Jr., W.E., 2007. Abiotic formation of hydrocarbons under hydrothermal conditions: Constraints from chemical and isotope data. Geochim. Cosmochim. Acta 71, 1982–1998.

Fu, B., Touret, J.L.R., Zheng, Y.F., 2003. Remnants of premetamorphic fluid and oxygen isotopic signatures in eclogites and garnet clinopyroxenite from the Dabie-Sulu teranes, eastern China. J. Metamorph. Geol. 21, 561–578.

Gao, J., Li, M.S., Xiao, X.C., Tang, Y.Q., He, G.Q., 1998. Paleozoic tectonic evolution of the Tianshan Orogen, northwestern China. Tectonophysics 287, 213–231.

Gerlach, T.M., 1980. Chemical characteristics of the volcanic gases from Nyiragongo Lava Lake and the generation of CH_4-rich fluid inclusions. J. Volcanol. Geoth. Res. 8, 177–189.

Giardini, A.A., Melton, C.E., Mitchell, R.S., 1982. The nature of the upper 400 km of the earth and its potential as the source for non-biogenic petroleum. J. Petrol. Geol. 5, 173–189.

Gize, A., Macdonald, R., 1993. Generation of compositionally atypical hydrocarbons in CO_2-rich geologic environments. Geology 21, 129–132.

Gold, T., 1979. Terrestrial sources of carbon and earthquake outgassing. J. Petrol. Geol. 1, 3–19.

Hall, D.L., Bodnar, R.J., 1990. Methane in fluid inclusions from granulites: a product of hydrogen diffusion? Geochim. Cosmochim. Acta 54, 641–651.

Hedenquist, J.W., Lowenstern, J.B., 1994. The role of magmas in the formation of hydrothermal ore deposits. Nature 370, 519–527.

Heinrich, C.A., 2005. The physical and chemical evolution of low-salinity magmatic fluids at the porphyry to epithermal transition: a thermodynamic study. Miner. Deposita 39, 864–889.

Horita, J., 2001. Carbon isotope exchange in the system CO_2-CH_4 at elevated temperatures. Geochim. Cosmochim. Acta 65, 1907–1919.

Horita, J., Berndt, M.E., 1999. Abiogenic methane formation and isotopic fractionation under hydrothermal conditions. Science 285, 1055–1057.

Hu, A.Q., Jahn, B.M., Zhang, G., Chen, Y., Zhang, Q., 2000. Crustal evolution and Phanerozoic crustal growth in northern Xinjiang: Nd isotopic evidence. Part I. Isotopic characterization of basement rocks. Tectonophysics 328, 15–51.

Hu, A.Q., Wei, G.J., Zhang, J.B., Deng, W.F., Chen, L.L., 2008. SHRIMP U-Pb ages for zircons of the amphibolites and tectonic evolution significance from the Wenquan domain in the West Tianshan Mountains, Xinjiang, China. Acta Petrol. Sin. 24, 2731–2740 (in Chinese with English abstract).

Hu, A.Q., Wei, G.J., Jahn, B.M., Zhang, J.B., Deng, W.F., Chen, L.L., 2010. Formation of the 0.9 Ga Neoproterozoic granitoids in the Tianshan Orogen, NW China: constraints from the SHRIMP zircon age determination and its tectonic significance. Geochimica 39, 197–212.

Kogarko, L.N., Kosztolanyi, C., Ryabchikov, I.D., 1987. Geochemistry of the reduced fluid in alkali magmas. Geochem. Int. 24, 20–27.

Kolesnikov, A., Kutcherov, V.G., Goncharov, A.F., 2009. Methane-derived hydrocarbons produced under upper-mantle conditions. Nat. Geosci. 2, 566–570.

Konnerup-Madsen, J., 2001. A review of the composition and evolution of hydrocarbon gases during solidification of the Ilímaussaq alkaline complex, South Greenland. Geol. Greenland Surv. Bull. 190, 159–166.

Krader, T., Franck, E.U., 1987. The ternary systems H_2O–CH_4–NaCl and H_2O–CH_4–$CaCl_2$ to 800 K and 250 MPa. Phys. Chem. Chem. Phys. 91, 627–634.

Lamb, W.M., Popp, R.K., Boockoff, L.A., 1996. The determination of phase relations in the CH_4·H_2O·NaCl system at 1 kbar, 400 to 600°C using synthetic fluid inclusions. Geochim. Cosmochim. Acta 60, 1885–1897.

Landtwing, M.R., Furrer, C., Redmond, P.B., Pettke, T., Guillong, M., Heinerich, C.A., 2010. The Bingham Canyon porphyry Cu-Mo-Au deposit. III. Zoned copper-gold ore deposition by magmatic vapor expansion. Econ. Geol. 105, 91–118.

Leybourne, M.I., Cameron, E.M., 2006. Composition of groundwaters associated with porphyry-Cu deposits, Atacama Desert, Chile: Elemental and isotopic constraints on water sources and water–rock reactions. Geochim. Cosmochim. Acta 70, 1616–1635.

Li, J., Chou, I.M., 2014. Hydrogen in silicate melt inclusions in quartz from granite detected with Raman spectroscopy. J. Raman. Spectrosc. 46, 983–986.

Liu, W., Fei, P.X., 2006. Methane-rich fluid inclusions from ophiolitic dunite and post-collisional mafic–ultramafic intrusion: The mantle dynamics underneath the Palaeo-Asian Ocean through to the post-collisional period. Earth Planet. Sci. Lett. 242, 286–301.

Liu, F., Zong, K.Q., Liu, Y.S., Hu, Z.C., Zhu, L.Y., Xu, R., 2015. Methane-bearing melt inclusion in olivine phenocryst in Cenozoic alkaline basalt from Eastern China and its geological significance. Chin. Sci. Bull. 60, 1310–1319 (in Chinese with English abstract).

Mao, W., Rusk, B., Yang, F.C., Zhang, M.J., 2017. Physical and chemical evolution of the Dabaoshan porphyry Mo deposit, South China: insights from fluid inclusions, cathodoluminescence, and trace elements in quartz. Econ. Geol. 112, 889–918.

Mountain, B.W., Seward, T.M., 2003. Hydrosulfide/sulfide complexes of copper(I): experimental confirmation of the stoichiometry and stability of Cu(HS)2− to elevated temperatures. Geochim. Cosmochim. Acta 67, 3005–3014.

Mungall, J.E., 2002. Roasting the mantle: slab melting and the genesis of major Au and Au-rich Cu deposits. Geology 30, 915–918.

Naney, M.T., 1983. Phase equilibria of rock-forming ferromagnesian silicates in granitic systems. Am. J. Sci. 283, 993–1033.

Ou, W., Guo, H., Lu, W., Wu, X., Chou, I.M., 2015. A re-evaluation of the effects of temperature and NaCl concentration on quantitative Raman spectroscopic measurements of dissolved CH_4 in NaCl aqueous solutions: application to fluid inclusion analysis. Chem. Geol. 417, 1–10.

Pearson, R.G., 1963. Hard and soft acids and their bases. J. Am. Chem. Soc. 85, 3533–3539.

Potter, J., Konnerup-Madsen, J., 2003. A review of the occurrence and origin of abiogenic hydrocarbons in igneous rocks. Geol. Soc. London Spec. Publ. 214, 151–173.

Potter, J., Rankin, A.H., Treloar, P.J., 2004. Abiogenic Fischer-Tropsch synthesis of hydrocarbons in alkaline igneous rocks; fluid inclusion, textural and isotopic evidence from the Lovozero complex, N.W. Russia. Lithos 75, 311–330.

Redmond, P.B., Einaudi, M.T., Inan, E.E., Landtwing, M.R., Heinrich, C.A., 2004. Copper deposition by fluid cooling in intrusion-centered systems: New insights from the Bingham porphyry ore deposit, Utah. Geology 32, 217–220.

Ren, T., Ma, M., 2015. Identification and significance of CH_4-rich fluid inclusions in Langdu skarn Cu deposit, Yunnan Province, China. J. Geol. Soc. India 86, 482–488.

Roedder, E., 1965. Liquid CO_2 inclusions in olivine-bearing nodules and phenocrysts from basalts. Am. Mineral. 50, 1746–1782.

Roedder, E., 1984. Fluid inclusions. Mineral. Soc. Am. Rev. Mineral. 12, 1–644.

Rollison, H., 1993. Using Geochemical Data: Evaluation, Presentation, Interpretation. Longman Scientific and Technical, Harlow, United Kingdom (GBR), pp. 1–380.

Rowins, S.M., 2000. Reduced porphyry copper-gold deposits: a new variation on an old theme. Geology 28, 491–494.

Rusk, B.G., Reed, M.H., Dilles, J.H., 2008. Fluid inclusion evidence for magmatic-hydrothermal fluid evolution in the porphyry copper-molybdenum deposit at Butte, Montana. Econ. Geol. 103, 307–334.

Salvi, S., Williams-Jones, A.E., 1997. Fischer-Tropsch synthesis of hydrocarbons during sub-solidus alteration of the Strange Lake peralkaline granite, Quebec/Labrador, Canada. Geochim. Cosmochim. Acta 61, 83–99.

Schoell, M., 1988. Multiple origins of methane in the Earth. Chem. Geol. 71, 1–10.

Scott, H.P., Hemley, R.J., Mao, H.K., Herschbach, D.R., Fried, L.E., Howard, W.M., Bastea, S., 2004. Generation of methane in the Earth's mantle: in situ high pressure-temperature measurements of carbonate reduction. Proc. Natl. Acad. Sci. U.S.A. 101, 14023–14026.

Seo, J.H., Guillong, M., Heinrich, C.A., 2009. The role of sulfur in the formation of magmatic-hydrothermal copper-gold deposits. Earth Planet. Sci. Lett. 282, 323–328.

Shen, P., Pan, H., 2013. Country-rock contamination of magmas associated with the

Baogutu porphyry Cu deposit, Xinjiang, China. Lithos 177, 451–469.
Shen, P., Shen, Y., Wang, J., Zhu, H., Wang, L., Meng, L., 2010. Methane-rich fluid evolution of the Baogutu porphyry Cu-Mo-Au deposit, Xinjiang, NW China. Chem. Geol. 275, 78–98.
Sherwood Lollar, B., Westgate, T.D., Ward, J.A., Slater, G.F., Lacrampe-Couloume, G., 2002. Abiogenic formation of alkanes in the Earth's crust as a minor source for global hydrocarbon reservoirs. Nature 416, 522–524.
Sherwood Lollar, B., Lacrampe-Couloume, G., Slater, G.F., Ward, J., Moser, D.P., Gihring, T.M., Lin, L.H., Onstott, T.C., 2006. Unravelling abiogenic and biogenic sources of methane in the Earth's deep subsurface. Chem. Geol. 226, 328–339.
Shi, G.U., Tropper, P., Cui, W., Tan, J., Wang, C., 2005. Methane (CH_4)-bearing fluid inclusions in the Myanmar jadeitite. Geochem. J. 39, 503–516.
Sillitoe, R.H., 2010. Porphyry copper systems. Econ. Geol. 105, 3–41.
Smith, C.M., Canil, D., Rowins, S.M., Friedman, R., 2012. Reduced granitic magmas in an arc setting: the Catface porphyry Cu-Mo deposit of the Paleogene Cascade Arc. Lithos 154, 361–373.
Stefanini, B., Williams-Jones, A.E., 1996. Hydrothermal evolution in the Calabona porphyry copper system (Sardinia, Italy); the path to an uneconomic deposit. Econ. Geol. 91, 774–791.
Sun, W.D., Liang, H.Y., Ling, M.X., Zhan, M.Z., Ding, X., Zhang, H., Yang, X.Y., Li, Y.L., Ireland, T.R., Wei, Q.R., 2013. The link between reduced porphyry copper deposits and oxidized magmas. Geochim. Cosmochim. Acta 103, 263–275.
Tang, G.J., Wang, Q., Wyman, D.A., Sun, M., Li, Z.X., Zhao, Z.H., Sun, W.D., Jia, X.H., Jiang, Z.Q., 2010. Geochronology and geochemistry of Late Paleozoic magmatic rocks in the Lamasu-Dabate area, northwestern Tianshan (west China): evidence for a tectonic transition from arc to post-collisional setting. Lithos 119, 393–411.
Tao, R.B., Zhang, L.F., Tian, M., Zhu, J.J., Liu, X., Liu, J.Z., Höfer, H.E., Stagno, V., Fei, Y.W., 2018. Formation of abiotic hydrocarbon from reduction of carbonate in subduction zone: constrints from petrological observation and experimental simulation. Geochim. Cosmochim. Acta 239, 390–408.
Taran, Y.A., Varley, N.R., Inguaggiato, S., Cienfuegos, E., 2010. Geochemistry of H_2- and CH_4- enriched hydrothermal fluids of Socorro Island, Revillagigedo Archipelago, Mexico. Evidence for serpentinization and abiogenic methane. Geofluids 10, 542–555.
Vasyukova, O.V., Williams-Jones, A.E., Blamey, N.J.F., 2016. Fluid evolution in the Strange Lake granitic pluton, Canada: implications for HFSE mobilisation. Chem. Geol. 444, 83–100.
Vitale Brovarone, A., Martinez, I., Elmaleh, A., Compagnoni, R., Chaduteau, C., Ferraris, C., Esteve, I., 2017. Massive production of abiotic methane during subduction evidenced in metamorphosed ophicarbonates from the Italian Alps. Nat. Commun. 8, 1–13.
Wang, B., Shu, L.S., Cluzel, D., Faure, M., Charvet, J., 2007. Geochemical constraints on Carboniferous volcanic rocks of the Yili Block (Xinjiang, NW China): implication for the tectonic evolution of Western Tianshan. J. Asian Earth. Sci. 29, 148–159.
Wang, L., Zhang, D., Tian, L., 2014. Silicate melt inclusions in the Qiushuwan granitoids, northern Qinling belt, China: implications for the formation of a porphyry Cu–Mo deposit as a reduced magmatic system. Cr. Geosci. 346, 190–199.
Whiticar, M.J., 1999. Carbon and hydrogen isotope systematics of bacterial formation and oxidation of methane. Chem. Geol. 161, 291–314.
Williams-Jones, A.E., Heinerich, C.A., 2005. Vapor transport of metals and the formation of magmatic-hydrothermal ore deposits. Econ. Geol. 100, 1287–1312.
Williams-Jones, A.E., Migdisov, A.A., 2014. Experimental constraints on the transport and seposition of metals in ore-forming hydrothermal systems. Econ. Geol. 18, 77–95.
XBGMR, 1993. In: Regional Geology of Xinjiang Uygur Autonomy Region. Geology Publishing House, Beijing, pp. 1–841.
Xiao, W.J., Windley, B.F., Allen, M.B., Han, C., 2013. Paleozoic multiple accretionary and collisional tectonics of the Chinese Tianshan orogenic collage. Gondwana. Res. 23, 1316–1341.
Xue, C.J., Chen, B., Jia, Z.Y., Zhang, B., Wan, Y., 2011. Geochemistry and chronology of Lailisigao'er-3571 porphyry Cu-Mo ore field, Western Tianshan, Xinjiang. Earth Sci. Front. 18, 149–165 (in Chinese with English abstract).
Zahnle, K.J., 1986. Photochemistry of methane and the formation of hydrocyanic acid (HCN) in the Earth's early atmosphere. J. Geophys. Res-Atmos. 91, 2819–2834.
Zhang, C., Duan, Z., 2010. GFluid: an Excel spreadsheet for investigating C-O–H fluid composition under high temperatures and pressures. Comput. Geosci.-UK 36, 569–572.
Zhang, W., Leng, C.B., Zhang, X.C., Su, W.C., Tang, H.F., Yan, J.H., Cao, J.L., 2016. Petrogenesis of the Seleteguole granitoids from Jinhe county in Xinjiang (West China): implications for the tectonic transformation of Northwest Tianshan. Lithos 256–257, 148–164.
Zhang, Z., Wang, Z., Zuo, G., Min, L., Wang, L., Wang, J., 2008. Ages and tectonic settings of the volcanic rocks in Dabate ore district in West Tianshan Mountains and their constraints on the porphyry-type mineralization. Acta Geol. Sin. 82, 1494–1503 (in Chinese with English abstract).
Zhu, M., Wu, G., Xie, H., Liu, J., Mei, M., 2012. Geochronology and fluid inclusion studies of the Lailisigaoer and Lamasu porphyry-skarn Cu-Mo deposits in Northwestern Tianshan, China. J. Asian Earth. Sci. 49, 116–130.
Zuo, G.C., Zhang, Z.H., Wang, Z.L., Liu, M., Wang, L.S., 2008. Tectonic division, stratigraphical stystem and the evolution of Western Tianshan Mountains, Xinjiang. Geol. Rev. 54, 748–767 (in Chinese with English abstract).